The Astrophysical Journal, 875:67 (17pp), 2019 April 10 https://doi.org/10.3847/1538-4357/ab07be

Results from EDGES High-Band. III. New Constraints on Parameters of the Early Universe

Raul A. Monsalve[1,2,3,4,5], Anastasia Fialkov[6,7,8,9,10], Judd D. Bowman[3], Alan E. E. Rogers[11], Thomas J. Mozdzen[3], Aviad Cohen[12], Rennan Barkana[12], and Nivedita Mahesh[3]

[1] Department of Physics, McGill University, Montréal, 3600 Rue University, QC H3A 2T8, Canada; Raul.Monsalve@mcgill.ca
[2] McGill Space Institute, McGill University, Montréal, 3550 Rue University, QC H3A 2A7, Canada
[3] School of Earth and Space Exploration, Arizona State University, 781 Terrace Mall, Tempe, AZ 85287, USA
[4] Center for Astrophysics and Space Astronomy, University of Colorado, 2000 Colorado Avenue, Boulder, CO 80309, USA
[5] Facultad de Ingeniería, Universidad Católica de la Santísima Concepción, Alonso de Ribera 2850, Concepción, Chile
[6] Harvard-Smithsonian Center for Astrophysics, Institute for Theory and Computation, 60 Garden Street, Cambridge, MA 02138, USA
[7] Institute of Astronomy, University of Cambridge, Madingley Road, Cambridge CB3 0HA, UK
[8] Kavli Institute for Cosmology, University of Cambridge, Madingley Road, Cambridge CB3 0HA, UK
[9] Department of Physics, The University of Tokyo, 7-3-1 Hongo, Bunkyo, Tokyo 113-0033, Japan
[10] Department of Physics and Astronomy, University of Sussex, Falmer, Brighton BN1 9QH, UK
[11] Haystack Observatory, Massachusetts Institute of Technology, 99 Millstone Road, Westford, MA 01886, USA
[12] Raymond and Beverly Sackler School of Physics and Astronomy, Tel Aviv University, Tel Aviv 69978, Israel
Received 2018 October 9; revised 2019 January 31; accepted 2019 February 14; published 2019 April 16

Abstract

We present new constraints on parameters of cosmic dawn and the epoch of reionization derived from the EDGES High-Band spectrum (90–190 MHz). The parameters are probed by evaluating global 21 cm signals generated with the recently developed `Global21cm` tool. This tool uses neural networks trained and tested on ∼30,000 spectra produced with semi-numerical simulations that assume the standard thermal evolution of the cosmic microwave background and the intergalactic medium. From our analysis, we constrain at 68% (1) the minimum virial circular velocity of star-forming halos to $V_c < 19.3\,\mathrm{km\,s^{-1}}$, (2) the X-ray heating efficiency of early sources to $f_X > 0.0042$, and (3) the low-energy cutoff of the X-ray spectral energy distribution to $\nu_{min} < 2.3$ keV. We also constrain the star formation efficiency (f_*), the electron scattering optical depth (τ_e), and the mean-free path of ionizing photons (R_{mfp}). We recompute the constraints after incorporating into the analysis four estimates for the neutral hydrogen fraction from high-z quasars and galaxies, and a prior on τ_e from *Planck* 2018. The largest impact of the external observations is on the parameters that most directly characterize reionization. Specifically, we derive the combined 68% constraints $\tau_e < 0.063$ and $R_{mfp} > 27.5$ Mpc. The external observations also have a significant effect on V_c due to its degeneracy with τ_e, while the constraints on f_*, f_X, and ν_{min}, remain primarily determined by EDGES.

Key words: cosmology: observations – early universe – galaxies: high-redshift – methods: data analysis

1. Introduction

The sky-averaged, or global, radio spectrum is expected to encode the redshift evolution of the 21 cm line of neutral hydrogen gas in the intergalactic medium (IGM) during the formation of the first stars and galaxies (Varshalovich & Khersonskii 1977; Tozzi et al. 2000; Barkana & Loeb 2001; Furlanetto et al. 2006; Pritchard & Loeb 2008). At the onset of star formation, stellar Lyα photons couple the spin temperature of the 21 cm signal to the temperature of the gas, a process that makes the line visible in absorption relative to the radio background radiation (Wouthuysen 1952; Field 1958). The detection by Bowman et al. (2018) of an absorption feature at ∼78 MHz, with a width of ∼20 MHz and an amplitude of ∼0.5 K, if confirmed to be of cosmological origin, is the first measurement of the 21 cm signal from cosmic dawn and would represent direct evidence of the formation of the first stars. The central frequency of the reported feature is in agreement with theoretical predictions and implies efficient star formation in halos of mass below $10^8\,M_\odot$ (Mirocha & Furlanetto 2019). Such a population would manifest itself in future high-redshift galaxy surveys generating a steeper-than-expected UV luminosity function at the faint end (Mirocha et al. 2017; Mirocha & Furlanetto 2019).

However, the amplitude and shape of the detected radio signal do not comply with standard models of cosmic dawn and reionization, where the absorption is measured against the cosmic microwave background (CMB) and the IGM is heated by X-ray sources after an initial period of adiabatic cooling (e.g., Mesinger et al. 2011; Cohen et al. 2017; Mirocha et al. 2018). The reported absorption amplitude is at least twice as large as predicted, and the observed shape is much flatter at the bottom than expected. These discrepancies have led to many suggestions of exotic physical mechanisms that could produce either a colder IGM temperature at early times (e.g., Tashiro et al. 2014; Muñoz et al. 2015; Barkana 2018; Barkana et al. 2018; Berlin et al. 2018; Fialkov et al. 2018; Hektor et al. 2018; Houston et al. 2018; Muñoz & Loeb 2018; Sikivie 2019) or a radiation background stronger than the CMB (e.g., Ewall-Wice et al. 2018; Feng & Holder 2018; Fraser et al. 2018).

Verification of the unexpected EDGES measurement, which was conducted with two "Low-Band" instruments observing in the 50–100 MHz frequency range ($26.4 \gtrsim z \gtrsim 13.2$), requires independent observations and constraints. Until the EDGES result, the only constraint on the global 21 cm signal from cosmic dawn in the same frequency range was the upper limit for the absorption amplitude of 0.89 K (95%) established by the LEDA experiment (Bernardi et al. 2016). Previously, the SCI-HI experiment reported upper limits in the range ∼1–10 K on the residual spectral structure after removing a model for the foreground contribution (Voytek et al. 2014). Upper limits on

the 21 cm power-spectrum signal have been presented in the range $z = 12$–18 by MWA (Ewall-Wice et al. 2016) and $z = 20$–25 by LOFAR (Gehlot et al. 2018). An additional, but also currently disputed, potential evidence of new physics at cosmic dawn could come from the measurement of the brightness temperature of the diffuse sky by ARCADE 2, which found a 54 mK "excess" above the CMB at 3.3 GHz (Fixsen et al. 2011). A consistent excess was recently reported using LWA1 data over 40–80 MHz (Dowell & Taylor 2018). However, the existence of this excess relies on the correct identification and removal of the Galactic and extragalactic contributions. Using a more realistic Galactic model, Subrahmanyan & Cowsik (2013) showed that the excess could instead correspond to a Galactic contribution that is not accounted for in other analyses.

Compared to cosmic dawn, constraints on the epoch of reionization are tighter and stem from several independent observational probes, none of which has so far reported deviations from traditional astrophysics. The average fraction of neutral hydrogen in the IGM, $\bar{x}_{\rm H\,I}$, can be constrained through the Lyα and Lyβ pixels that are dark in the spectra of high-z quasars. Using this technique and a sample of 22 quasars at $z = 5$–6, McGreer et al. (2015) derive the upper limit $\bar{x}_{\rm H\,I} \leqslant 0.06 + 0.05$ (68%) at $z = 5.9$. Neutral hydrogen in the IGM also imprints a "damping wing" absorption feature in the spectrum of high-z quasars. Greig et al. (2017) obtain $\bar{x}_{\rm H\,I} = 0.40^{+0.21}_{-0.19}$ (68%) from the damping wing analysis of ULASJ1120+0641, showing that reionization is ongoing at $z = 7.08$; while the spectrum of ULASJ1342+0928, the highest-redshift quasar detected so far, yields $\bar{x}_{\rm H\,I} = 0.65^{+0.15}_{-0.32}$ (68%) at $z = 7.54$ in a damping wing analysis by Bañados et al. (2018). The IGM neutral fraction can also be constrained from the emission of Lyα radiation from Lyman break galaxies (LBGs). In a Bayesian analysis that incorporates reionization simulations and empirical models of the interstellar medium, Mason et al. (2018) determine $\bar{x}_{\rm H\,I} = 0.59^{+0.11}_{-0.15}$ (68%) at $z = 7$ from a sample of LBGs presented in Pentericci et al. (2014). CMB fluctuations provide an independent test of reionization by probing the integrated electron scattering optical depth to recombination, $\tau_{\rm e}$. Among other values, the *Planck* satellite recently reported $\tau_{\rm e} = 0.056 \pm 0.007$, which corresponds to a reionization center redshift $z = 7.82 \pm 0.71$ assuming a "tanh" phenomenological model (Planck Collaboration VI 2018). For a similar type of model, the data from the EDGES "High-Band" instrument provide independent constraints on the reionization duration (Δz) via non-detection of the 21 cm line in the 90–190 MHz range (Monsalve et al. 2017b): at $\geqslant 2\sigma$ significance, the data rule out models with $\Delta z < 1$ at $z \sim 8.5$ and higher than $\Delta z = 0.4$ across most of the $14.8 \geqslant z \geqslant 6.5$ range. These constraints implicitly correspond to reionization scenarios where the 21 cm spin temperature of neutral hydrogen is saturated, i.e., much higher than the microwave background, due to prior IGM heating. Monsalve et al. (2017b) also explored and ruled out 21 cm models that take the opposite extreme assumption, i.e., total Lyα coupling but no IGM heating before reionization. In this case, the hydrogen neutral fraction was also modeled using the "tanh" expression. As a reference result, Monsalve et al. (2017b) ruled out at $\geqslant 2\sigma$ all the reionization models with total Lyα coupling but no IGM heating that produce $\bar{x}_{\rm H\,I} \leqslant 1\%$ at $z = 6$ and have an optical depth in the range $0.086 \geqslant \tau_{\rm e} \geqslant 0.038$. Finally, there are also constraints on the 21 cm power-spectrum signal at $z = 8.6$ from GMRT (Paciga et al. 2013) and at $z = 7.1$ from MWA (Beardsley et al. 2016), while the tightest upper limits have been reported by LOFAR in the range $z = 9.6$–10.6 (Patil et al. 2017).[13]

Recently, global radio spectra were analyzed using astrophysical models for the first time (Singh et al. 2017, 2018; Monsalve et al. 2018). A set of 193 models from a parameter study by Cohen et al. (2017) was evaluated using data from the SARAS 2 experiment in the 110–200 MHz band, which allowed to rule out, at $>5\sigma$ significance, 25 models that share inefficient X-ray heating and rapid reionization (Singh et al. 2017, 2018). A much broader study was done using EDGES High-Band data (Monsalve et al. 2018, M18 hereafter), which evaluated 10,000 models generated with the `21cmFAST` code (Mesinger & Furlanetto 2007; Mesinger et al. 2011). M18 constrained the following parameters of cosmic dawn and reionization: the minimum virial temperature ($T_{\rm vir}^{\rm min}$) and ionizing efficiency (ζ) of star-forming halos, as well as the integrated soft-band X-ray luminosity ($L_{\rm X<2\,keV}/{\rm SFR}$) and threshold energy for self-absorption (E_0) of the first galaxies. For reference, using EDGES data alone, M18 disfavored (68%) $\log_{10}(T_{\rm vir}^{\rm min}/{\rm K}) > 5.5$ and $\zeta > 154.6$, as well as the intermediate range of X-ray luminosity $38.8 < \log_{10}(L_{\rm X<2\,keV}/{\rm SFR}/{\rm erg\ yr\ s^{-1}}\ M_\odot^{-1}) < 40.4$. Further, combining (1) the EDGES High-Band data, (2) an estimate for $\tau_{\rm e}$ from *Planck* 2016, and (3) constraints on $\bar{x}_{\rm H\,I}$ from quasars at $z = 5.9$ and $z = 7.08$ resulted in significantly stronger constraints on ζ and $T_{\rm vir}^{\rm min}$, with EDGES contributing to produce slightly better results than those derived in Greig & Mesinger (2017a) using only the information on $\tau_{\rm e}$ and $\bar{x}_{\rm H\,I}$.

In this paper we use the EDGES High-Band data to evaluate a different set of astrophysical models, which were generated with the `Global21cm` global signal emulator described in detail by A. Cohen et al. (2019, in preparation). This tool is based on neural networks trained on 29,641 outputs of semi-numerical simulations of cosmic dawn and reionization described in detail in Visbal et al. (2012), Fialkov & Barkana (2014), and Cohen et al. (2017). The simulations make standard assumptions for the temperatures of the CMB and the IGM, not taking into account the exotic physics invoked to explain the EDGES Low-Band result. To produce the simulations, seven astrophysical parameters were varied in the widest possible range: the minimum virial circular velocity of star-forming halos ($V_{\rm c}$), the star formation efficiency (SFE) (f_*), the X-ray heating efficiency of early sources ($f_{\rm X}$), the low-energy cutoff ($\nu_{\rm min}$) of the X-ray spectral energy distribution (SED), the slope (α) of the X-ray SED, the mean-free path of ionizing photons ($R_{\rm mfp}$), and $\tau_{\rm e}$. `Global21cm` interpolates between the outputs of the semi-numerical simulations and produces global signals for any combination of parameters.

Here, we generate 6.4 million global signals using `Global21cm` and conduct a Bayesian analysis that rigorously maps the posterior probability density function (PDF) of six of the astrophysical parameters: $V_{\rm c}, f_*, f_{\rm X}, \nu_{\rm min}, R_{\rm mfp}$, and $\tau_{\rm e}$. We fix the value of α as it only mildly affects the results. We derive constraints on the parameters first using the EDGES High-Band data alone, and then combining them with a prior on $\tau_{\rm e}$ from *Planck* and constraints on $\bar{x}_{\rm H\,I}$ from high-z quasars and galaxies. Our main results are the 1D and 2D PDFs of each parameter and parameter pair, obtained after marginalizing over

[13] The PAPER 21 cm power-spectrum constraint at $z = 8.4$ of Ali et al. (2015) has been retracted in Ali et al. (2018).

the rest of the astrophysical parameters as well as the parameters that account for the contribution of diffuse foregrounds to the radio spectrum.

In addition to exploring more parameters, six instead of four, we improve on M18 by including in our combined analysis an updated prior on τ_e (*Planck* 2018 instead of 2016), a constraint on $\bar{x}_{\rm H\,I}$ at $z = 7.54$ by Bañados et al. (2018) from the ULASJ1342+0928 quasar, and a constraint on $\bar{x}_{\rm H\,I}$ at $z = 7$ by Mason et al. (2018) from LBGs. In general, the parameters we explore are different from those in M18, and although some of them overlap, here we explore them over a wider range. This makes it difficult to compare in detail our results with those of M18. On the other hand, it enables us to derive independent conclusions about the astrophysics of the early universe. As in M18, we do not incorporate the EDGES Low-Band spectrum into our analysis, saving that for future work.

The paper is organized as follows. In Section 2 we briefly describe the 21 cm astrophysical parameters. In Section 3 we detail our analysis procedure. In Section 4 we present the results obtained from the analysis of EDGES data alone, the external constraints alone, and their combination. In Section 5 we discuss the results and compare them with those for models from `21cmFAST`. Finally, in Section 6 we summarize this work.

2. Astrophysical Parameters

The `Global21cm` code outputs a global 21 cm signal over the redshift range $6 < z < 50$ given a combination of key astrophysical parameters in less than one second of computing time. The code employs neural networks that were trained on 29,641 global spectra produced with a hybrid simulation of the high-redshift universe (Visbal et al. 2012; Fialkov & Barkana 2014; Cohen et al. 2017). For an input set of astrophysical parameters, the simulation generates a realization of the 21 cm signal within large cosmological volumes (384^3 comoving Mpc^3) and over a wide redshift range ($z = 6$–60). The global spectra are obtained by averaging the 3D 21 cm fields over the box at every redshift. Each simulation takes $\sim$4 hr to run on a desktop, and the ensemble of 29,641 models was produced using the *Odyssey* cluster at Harvard University.[14] All these runs were executed with the same set of initial conditions for large-scale density and velocity fields at $z = 60$, and assume ΛCDM with the standard cosmological parameters (Planck Collaboration XVI 2014). The simulation follows the hierarchical growth of structure, tracks star formation averaged over scales of $\sim$3 Mpc, and follows the evolution of inhomogeneous Lyα, Lyman–Werner (11.2–13.6 eV), X-ray, and ionizing radiative backgrounds. The simulation takes into account the effect of relative streaming velocity (Visbal et al. 2012), Lyman–Werner radiation (Fialkov et al. 2013), and photoheating feedback on star formation (Cohen et al. 2016).

In the simulation, the high-redshift astrophysics is parameterized with seven parameters: V_c, f_*, f_X, $\nu_{\rm min}$, α, $R_{\rm mfp}$, and ζ. The `Global21cm` code receives as input the same parameters except for ζ; the code uses instead the CMB optical depth, which is related to ζ by a one-to-one mapping. In the rest of this section we briefly describe the parameters and their impact on the global signal. For detailed descriptions we point the reader to Cohen et al. (2017) and A. Cohen et al. (2019, in preparation). An example is given in Figure 1, where

[14] https://www.rc.fas.harvard.edu/odyssey/

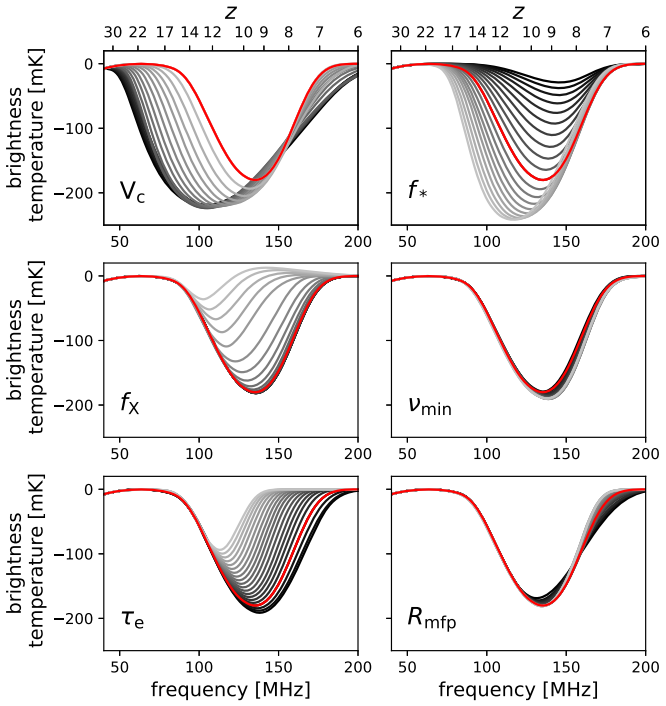

Figure 1. Example of dependence of the global 21 cm signal on the parameters constrained. The signals are produced using the `Global21cm` code (A. Cohen et al. 2019, in preparation). Each panel shows variations in one parameter relative to a common reference. The colors of the signals, from black to light gray, represent the parameter value going from lowest to highest, spanning the ranges described in Section 2 and listed in Table 1. For V_c, f_*, and f_X, the sampling is done evenly in $\log_{10}$ scale. The red signal is the common reference, with parameters $V_c = 76.5$ km s^{-1}, $f_* = 0.026$, $f_X = 3.4 \times 10^{-3}$, $\nu_{\rm min} = 0.25$ keV, $\tau_e = 0.06$, and $R_{\rm mfp} = 31$ Mpc.

Table 1
Parameter Ranges and Sampling Scale

Parameter	Min	Max	Unit	Scale
V_c	4.2	76.5	km s^{-1}	$\log_{10}$
f_*	10^{-3}	0.5	⋯	$\log_{10}$
f_X	10^{-5}	10	⋯	$\log_{10}$
$\nu_{\rm min}$	0.1	3	keV	linear
τ_e	0.055	0.09	⋯	linear
$R_{\rm mfp}$	10	50	Mpc	linear

we show the effect of changes in all the parameters except α, which is kept fixed at $\alpha = -1.3$. In Table 1 we list the parameter ranges explored in this paper, as well as the scale used to sample these ranges with `Global21cm`. Although our parameterization intends to characterize the large-scale physics of cosmic dawn and reionization, it is not necessarily optimized for the global 21 cm signal. Therefore, the effect of some of the parameters on the global signal is degenerate. We discuss this point in Section 5.1.

Minimum virial circular velocity. In the hierarchical picture of structure formation, low-mass halos form at higher redshifts and are more numerous than high-mass halos. Therefore, in the cases with lower threshold mass for star formation, $M_{\rm min}$, stars form earlier, leading to an earlier onset of the Lyα coupling and shifting the descending slope of the 21 cm absorption feature to lower frequencies. In `Global21cm` we use the minimum

virial circular velocity,

$$V_c \sim 16.9\left(\frac{M_{\rm min}}{10^8}\right)^{1/3}\left(\frac{1+z}{10}\right)^{1/2}\ {\rm km\ s^{-1}}, \quad (1)$$

instead of $M_{\rm min}$ because V_c is less strongly dependent on redshift (Barkana 2016).

V_c is primarily set by the cooling channel. Molecular hydrogen cooling fuels star formation in halos with $V_c = 4.2$–$16.5\ {\rm km\ s^{-1}}$, which corresponds to halo masses $M_h \sim 1\times10^6$–$8\times10^7\ M_\odot$ at $z = 10$, while atomic hydrogen cooling occurs for $V_c > 16.5\ {\rm km\ s^{-1}}$ (Barkana 2016). In addition to radiative cooling, star formation is affected by numerous feedback processes that result in spatial variation of V_c as well as in its dependence on background radiation fields (e.g., Machacek et al. 2001; Fialkov et al. 2012, 2013). To probe different cooling and feedback mechanisms, in this paper we vary V_c in a broad range, from $4.2\ {\rm km\ s^{-1}}$, corresponding to the minimum value for molecular hydrogen cooling, to $76.5\ {\rm km\ s^{-1}}$, representing atomic hydrogen cooling and inefficient star formation in smaller halos due to, e.g., supernovae feedback.

Star formation efficiency. The SFE corresponds to the fraction of gas in dark matter halos that is converted into stars. Higher values of SFE result in an earlier onset of Lyα coupling, as well as in a faster build-up of X-ray and ionizing radiation backgrounds. The SFE depends on feedback mechanisms, the metalicity of the gas, and the halo mass. Star formation simulations in metal-poor environments show large scatter, with an SFE between ∼0.1% and ∼10% in halos of $M_h \sim 10^8$–$10^{10}\ M_\odot$ at $z \sim 10$ (e.g., Xu et al. 2016; Ceverino et al. 2017; Ma et al. 2018). Abundance matching techniques applied to $z \geqslant 6$ galaxies find that the SFE peaks at ∼30% for halos of $M_h \sim 10^{11}$–$10^{12}\ M_\odot$, dropping to ∼10% at $M_h \sim 10^{10}\ M_\odot$ and $M_h \sim 10^{13}\ M_\odot$ (Behroozi & Silk 2015; Mason et al. 2015; Mashian et al. 2016; Sun & Furlanetto 2016; Mirocha et al. 2017). Finally, observations of dwarf galaxies infer an SFE ∼ 0.01%–0.1% at $z \sim 10$ (Read et al. 2016).

We use the following SFE-M_h dependence for the models in this study (Cohen et al. 2017):

$$\mathrm{SFE}(M_h) = \begin{cases} f_* & M_{\rm atomic} < M_h, \\ f_*\dfrac{\log(M_h/M_{\rm min})}{\log(M_{\rm atomic}/M_{\rm min})} & M_{\rm min} < M_h < M_{\rm atomic}, \\ 0 & M_h < M_{\rm min}, \end{cases} \quad (2)$$

where $M_{\rm min}$ is the minimum cooling mass of star-forming halos, $M_{\rm atomic}$ is the minimum halo mass for atomic cooling, and f_* is a parameter that stands for the SFE at the high-mass end. We vary f_* over the wide range 0.1%–50%.

X-ray SED low-frequency cutoff. The process of IGM X-ray heating can be characterized in terms of the shape of the X-ray SED and the total luminosity. The IGM heating rate, and thus the evolution of the gas temperature, depends on the amount of energy injected by X-ray sources below ∼2 keV. Dust in host galaxies prevents soft X-rays below $\mathcal{O}(0.1)$ keV from penetrating the IGM, imposing a low-energy cutoff in the spectrum of the injected photons (e.g., Das et al. 2017). On the other hand, hard X-rays are barely absorbed; they free-stream and add up to form an X-ray background.

In `Global21cm` we model the X-ray SED as a power law with slope α and low-energy cutoff $\nu_{\rm min}$. However, we find that variations in α lead to very weak variations of the global signal relative to the sensitivity of the EDGES High-Band data. Therefore, here we fix the value of α at −1.3. Higher values of $\nu_{\rm min}$ lead to the effective hardening of the X-ray SED, less efficient heating, and, as a result, deeper 21 cm absorption with a higher central frequency. This scenario resembles the effect of X-ray binaries (XRBs), one of the most plausible sources to dominate high-redshift X-ray emission. XRBs are expected to have a hard X-ray SED that peaks at ∼1–3 keV and has a high-energy tail following a power law with slope $\alpha \sim -1.5$ (Mirabel et al. 2011; Fragos et al. 2013). We vary $\nu_{\rm min}$ in the range 0.1–3 keV, which is wide enough to explore the effects of host galaxy absorption as well as hard X-rays.

X-ray efficiency. The total X-ray luminosity of early sources satisfies the following relation, derived from observations of nearby starburst galaxies and XRBs (Grimm et al. 2003; Gilfanov et al. 2004; Mineo et al. 2012):

$$\frac{L_X}{\rm SFR} = 3\times10^{40} f_X\ {\rm erg\ s^{-1}}\ M_\odot^{-1}\ {\rm yr}, \quad (3)$$

where L_X is the total X-ray luminosity emitted in the range $\nu_{\rm min}$ − 95 keV, SFR is the star formation rate (which in our parameterization is a function of M_h, f_*, and z, as well as of the large-scale overdensity and relative velocity between dark matter and gas), and f_X is the X-ray efficiency of sources, which is our parameter in `Global21cm`. Fialkov et al. (2017) found that the unresolved soft X-ray background measured by the *Chandra X-ray observatory* (Lehmer et al. 2012) imposes an upper limit on f_X in the range ∼10–500, depending on the nature of the X-ray sources, the halo cooling channel, and the reionization history. For high values of f_X, the contribution of X-rays to reionization becomes significant (up to ∼50% in the case with $f_X = 422$ and $\nu_{\rm min} = 0.2$ keV, Fialkov et al. 2017), and the absorption trough is shallow and occurs at low frequencies. Low values of f_X result in deep absorption troughs centered at high frequencies. This has made it possible to exclude models with low f_X (for some values of V_c and f_*) using SARAS 2 data (Singh et al. 2017, 2018). Here we vary f_X over the wide range 10^{-5}–10.

Mean-free path of ionizing photons. During reionization, the distance to which ionizing photons can propagate into the IGM determines the physical size of ionized regions. This distance depends on the abundance, density, and structure of photon sinks—absorption systems such as Lyman limit systems, and the corresponding recombinations of these systems. In our parameterization we explore the mean-free path of ionizing photons, $R_{\rm mfp}$, which we vary over 10–50 Mpc (Alvarez & Abel 2012; Greig & Mesinger 2017b). The effect of this parameter is only manifested after the onset of reionization. Higher values of $R_{\rm mfp}$ lead to a faster reionization and a steeper 21 cm signal at the high-frequency end, which can be constrained by EDGES High-Band.

Electron scattering optical depth. The last independent parameter is the ionizing efficiency of sources, ζ (Greig & Mesinger 2017a, M18). However, because CMB experiments probe the CMB optical depth instead of ζ, `Global21cm` was constructed to receive τ_e instead of ζ as an input parameter. The CMB optical depth measures the total column density of ionized gas, and is thus a function of the reionization history, $\bar{x}_{\rm H\,I}$, which

is inferred from the simulations and depends on all the astrophysical parameters. Given the evolution of $\bar{x}_{\rm H\,I}$ with redshift and for a mass-independent ionizing efficiency, we find a one-to-one relation between ζ and $\tau_{\rm e}$. The mapping between these two parameters is done using a neural network that was trained on a set of 27,455 cases and tested with 2186 cases (A. Cohen et al. 2019, in preparation). Increasing $\tau_{\rm e}$ while keeping the other parameters fixed amounts to a higher ζ and a faster depletion of neutral gas. This results in an earlier reionization and a shallower 21 cm absorption with the trough shifted to lower frequencies, as well as a reduced emission feature if such exists. Sixty-eight percent confidence constraints from the *Planck* 2016 release include $\tau_{\rm e} = 0.066 \pm 0.016$, 0.078 ± 0.019 (Planck Collaboration XIII 2016), 0.055 ± 0.009 (Planck Collaboration XLVI 2016), and 0.058 ± 0.012 (Planck Collaboration XLVII 2016). Considering these estimates, we explore the range $\tau_{\rm e} =$ 0.055–0.09. The lower limit of the range, $\tau_{\rm e} = 0.055$, was determined from the upper limit on $\bar{x}_{\rm H\,I}$ reported by McGreer et al. (2015), of $\bar{x}_{\rm H\,I} \leqslant 0.06 + 0.05$ (68%) at $z = 5.9$. For our `Global21cm` models, this upper limit results in a <1% probability for $\tau_{\rm e} < 0.056$ when considering the range $\tau_{\rm e} = 0.055$–0.09 (see Section 4.3). In Section 4.2 we discuss how new 2018 results from high-z galaxies (Mason et al. 2018) and *Planck* (Planck Collaboration VI 2018) warrant extending the range to lower values of $\tau_{\rm e}$ in future studies. The upper limit of our range, $\tau_{\rm e} = 0.09$, is high considering current constraints. However, exploring a wide range is useful because $\tau_{\rm e}$ is model-dependent and our $\bar{x}_{\rm H\,I}$ models do not correspond to those that were used by *Planck*.

3. Analysis

Exploring rigorously the parameter space of six dimensions described in Section 2 with high resolution is computationally expensive. Considering the low sensitivity of the global 21 cm signal to changes in $\nu_{\rm min}$ and $R_{\rm mfp}$, we explore the six parameters by dividing the space into two subsets of five parameters each. In one subset, the fifth parameter is $\nu_{\rm min}$ and $R_{\rm mfp}$ is fixed at 30 Mpc. In the other subset, the fifth parameter is $R_{\rm mfp}$ and $\nu_{\rm min}$ is fixed at 0.5 keV. We generate the 21 cm signals by evaluating the `Global21cm` code at 20 values per parameter over a regular grid in the ranges described in Section 2 and Table 1. This produces a total of $20^5 = 3.2$ million models for each five-parameter set. Because of their large dynamic ranges, the sampling for $V_{\rm c}$, f_*, and $f_{\rm X}$ is done in $\log_{10}$ scale, while $\tau_{\rm e}$, $\nu_{\rm min}$, and $R_{\rm mfp}$ are sampled in linear scale.

Following M18, we constrain the parameters by computing their marginalized posterior PDFs within a Bayesian framework. We first derive constraints using EDGES data alone, and then incorporating into the analysis external estimates for $\tau_{\rm e}$ and $\bar{x}_{\rm H\,I}$. We describe the analyses next.

3.1. EDGES-only Analysis

In the EDGES-only analysis we start by fitting our model for the diffuse foregrounds to the difference $d - m_{21}(\boldsymbol{\theta}_{21})$, where d is the spectrum measured by EDGES in the range 90–190 MHz (Monsalve et al. 2017b) and $m_{21}(\boldsymbol{\theta}_{21})$ represents each 21 cm signal that is produced by evaluating `Global21cm` at the vector of 21 cm astrophysical parameters $\boldsymbol{\theta}_{21}$. The diffuse foreground model is given by (Mozden et al. 2016; Monsalve et al. 2017a, 2017b, M18)

$$m_{\rm fg}(\boldsymbol{\theta}_{\rm fg}) = \sum_{i=0}^{N_{\rm fg}-1} a_i \nu^{-2.5+i} = A\boldsymbol{\theta}_{\rm fg}, \tag{4}$$

where ν is frequency, $N_{\rm fg} = 5$ is the number of foreground terms needed to fit the spectrum over 100 MHz (Monsalve et al. 2017b, M18), A is a matrix with columns corresponding to the $\nu^{-2.5+i}$ basis functions, and $\boldsymbol{\theta}_{\rm fg}$ is the vector of foreground polynomial coefficients with elements a_i.

We fit Equation (4) to $d - m_{21}(\boldsymbol{\theta}_{21})$ using least squares. The best-fit foreground parameters and model are denoted as $\hat{\boldsymbol{\theta}}_{\rm fg}$ and $\hat{m}_{\rm fg}$, respectively. The uncertainty of $\hat{\boldsymbol{\theta}}_{\rm fg}$ is encapsulated in their 5×5 covariance matrix, $C = (A^T \Sigma^{-1} A)^{-1}$, where Σ is the $N_\nu \times N_\nu$ covariance matrix of the measured spectrum and N_ν is the number of spectral channels. We construct Σ as a diagonal matrix where each element on the diagonal is the sum of the channel variance due to thermal noise and systematic uncertainty. For our channel width of 390.6 kHz, the standard deviation of the thermal noise is ≈40, 6, and 3 mK at 90, 140, and 190 MHz, respectively. The systematic uncertainty estimate has a standard deviation of 35 mK (M18). Finally, the $N_\nu \times N_\nu$ covariance matrix of $\hat{m}_{\rm fg}$ is given by $\Sigma_{\rm fg} = ACA^T$.

With the definitions above, and as derived in M18, the likelihood of the data as a function of $\boldsymbol{\theta}_{21}$ after marginalizing over the uncertainty of $\hat{\boldsymbol{\theta}}_{\rm fg}$ is given by

$$\mathcal{L}(d|\boldsymbol{\theta}_{21}) = \sqrt{\frac{(2\pi)^{N_{\rm fg}-N_\nu}}{|\Sigma||C^{-1}|}} \exp\left\{-\frac{1}{2}[d - m_{21}(\boldsymbol{\theta}_{21}) - \hat{m}_{\rm fg}]^T \times (\Sigma + V)^{-1}[d - m_{21}(\boldsymbol{\theta}_{21}) - \hat{m}_{\rm fg}]\right\}, \tag{5}$$

where $V = (\Sigma_{\rm fg}^{-1} - \Sigma^{-1})^{-1}$. This likelihood is evaluated for each of the 6.4 million global signals produced with `Global21cm`. Defining the prior distribution of the $\boldsymbol{\theta}_{21}$ parameters as $\mathcal{P}(\boldsymbol{\theta}_{21})$, the 1D and 2D posterior PDFs are obtained by numerically integrating the product $\mathcal{L}(d|\boldsymbol{\theta}_{21})\mathcal{P}(\boldsymbol{\theta}_{21})$ over the $\boldsymbol{\theta}_{21}$ parameters being marginalized. In the EDGES-only analysis we assume a uniform prior distribution for all the parameters over the ranges listed in Table 1 (uniform in $\log_{10}$ for $V_{\rm c}$, f_*, and $f_{\rm X}$, and in linear scale for the others).

3.2. Combined Analysis

Following Greig & Mesinger (2017a) and M18, and improving over M18 by using a more recent prior on $\tau_{\rm e}$ and two additional constraints on $\bar{x}_{\rm H\,I}$, we derive constraints on the high-z astrophysical parameters after incorporating into our analysis the following external estimates:

1. $\tau_{\rm e}$ estimate from *Planck*: We use as a prior the estimate $\tau_{\rm e} = 0.056 \pm 0.007$ (68%) from Planck Collaboration VI (2018), which we model as Gaussian. Planck Collaboration VI (2018) report several values, including the baseline result $\tau_{\rm e} = 0.054 \pm 0.007$ derived from the analysis that considers the *Planck* CMB power spectra and lensing reconstruction. Here we choose to use $\tau_{\rm e} = 0.056 \pm 0.007$, obtained from the analysis that also incorporates baryon acoustic oscillation measurements.
2. $\bar{x}_{\rm H\,I}$ constraint at $z = 5.9$: We use the upper limit on $\bar{x}_{\rm H\,I}$ from McGreer et al. (2015), derived from the fraction of

pixels that are dark in the Lyα and Lyβ regions of high-z quasar spectra (Mesinger 2010). We model this upper limit as a flat probability for $\bar{x}_{\rm H\,I} \leqslant 0.06$ and a decreasing probability for $\bar{x}_{\rm H\,I} > 0.06$, which follows a Gaussian with center $\bar{x}_{\rm H\,I} = 0.06$ and width $\sigma = 0.05$.

3. $\bar{x}_{\rm H\,I}$ estimate at $z = 7.08$: We use the $\bar{x}_{\rm H\,I}$ PDF estimated by Greig et al. (2017) from the Lyα damping wing analysis of the ULASJ1120+0641 quasar (Mortlock et al. 2011). Specifically, we use their result for the "Small H II" reionization morphology (Mesinger et al. 2016). From this PDF, the 68% estimate is $\bar{x}_{\rm H\,I} = 0.40^{+0.21}_{-0.19}$.
4. $\bar{x}_{\rm H\,I}$ estimate at $z = 7.54$: We use the most conservative (i.e., widest) $\bar{x}_{\rm H\,I}$ PDF estimated by Bañados et al. (2018) from the Lyα damping wing analysis of the ULASJ1342+0928 quasar. This estimate accounts for uncertainty in the quasar's intrinsic emission through numerical simulations normalized to the average continuum emission of analog quasars in the Sloan Digital Sky Survey quasar catalog (Pâris et al. 2017). From this PDF, the 68% estimate is $\bar{x}_{\rm H\,I} = 0.65^{+0.15}_{-0.32}$.
5. $\bar{x}_{\rm H\,I}$ estimate at $z = 7$: We use the $\bar{x}_{\rm H\,I}$ PDF computed by Mason et al. (2018) in their analysis of Lyα transmission from the 68 LBGs reported by Pentericci et al. (2014). Their analysis incorporates reionization simulations and empirical models of radiative transfer effects in the interstellar medium, yielding the 68% estimate $\bar{x}_{\rm H\,I} = 0.59^{+0.11}_{-0.15}$.

The PDFs corresponding to these constraints are depicted in Figure 2. We consider the *Planck* $\tau_{\rm e}$ PDF a prior because it corresponds to a parameter directly explored in our analysis. This PDF enters into our analysis through $\mathcal{P}(\tau_{\rm e})$. The other constraints are incorporated through an additional likelihood factor, $\mathcal{L}(\bar{x}_{\rm H\,I}|\boldsymbol{\theta}_{21})$, that multiplies the product $\mathcal{L}(d|\boldsymbol{\theta}_{21})\mathcal{P}(\boldsymbol{\theta}_{21})$. $\mathcal{L}(\bar{x}_{\rm H\,I}|\boldsymbol{\theta}_{21})$ is obtained by evaluating the $\bar{x}_{\rm H\,I}$ PDFs at the values of $\bar{x}_{\rm H\,I}$ produced by `Global21cm` at $z = 5.9$, 7.08, and 7.54, for every combination of $\boldsymbol{\theta}_{21}$ parameters.

The quasar constraints on $\bar{x}_{\rm H\,I}$ from McGreer et al. (2015) and Greig et al. (2017) account for sigthline-to-sightline variance. Specifically, McGreer et al. (2015) conduct a jackknife analysis where $\bar{x}_{\rm H\,I}$ is estimated repeatedly after removing one quasar at a time from their 22-quasar sample. Greig et al. (2017) estimate this effect by computing the $\bar{x}_{\rm H\,I}$ PDF for 10^5 sightlines extracted from semi-numerical reionization simulations (Mesinger et al. 2016). Recently, Davies et al. (2018) conducted an independent analysis of J1120+0641 ($z = 7.08$) that accounts for intrinsic emission uncertainty and sightline variance and obtained the estimate $\bar{x}_{\rm H\,I} = 0.48 \pm 0.26$ (68%), which is consistent with Greig et al. (2017) at $<1\sigma$. The constraint inferred by Mason et al. (2018) from LBGs is tighter than those from J1120+0641 by Greig et al. (2017) and Davies et al. (2018) at the same redshift, while consistent at the $\sim 1\sigma$ level. This provides support for an ongoing reionization at $z \approx 7$. We choose to include both $z \approx 7$ constraints (J1120+0641 and LBGs) in our analysis because they are completely independent and, when combined, are expected to produce a more precise and representative estimate of the average fraction of neutral hydrogen.

The constraint from J1342+0928 ($z = 7.54$) in Bañados et al. (2018) used in this paper only accounts for uncertainty in the quasar's intrinsic emission and does not incorporate the effect of sightline variance. However, we still treat this constraint as representative at $z = 7.54$ because in addition to being their most conservative result, the sightline variance for a significantly neutral IGM is expected to be smaller than for lower neutral hydrogen fractions (McGreer et al. 2011). The same quasar was analyzed by Davies et al. (2018) including the sightline variance effect. They obtained $\bar{x}_{\rm H\,I} = 0.60^{+0.20}_{-0.23}$ (68%), consistent with Bañados et al. (2018).

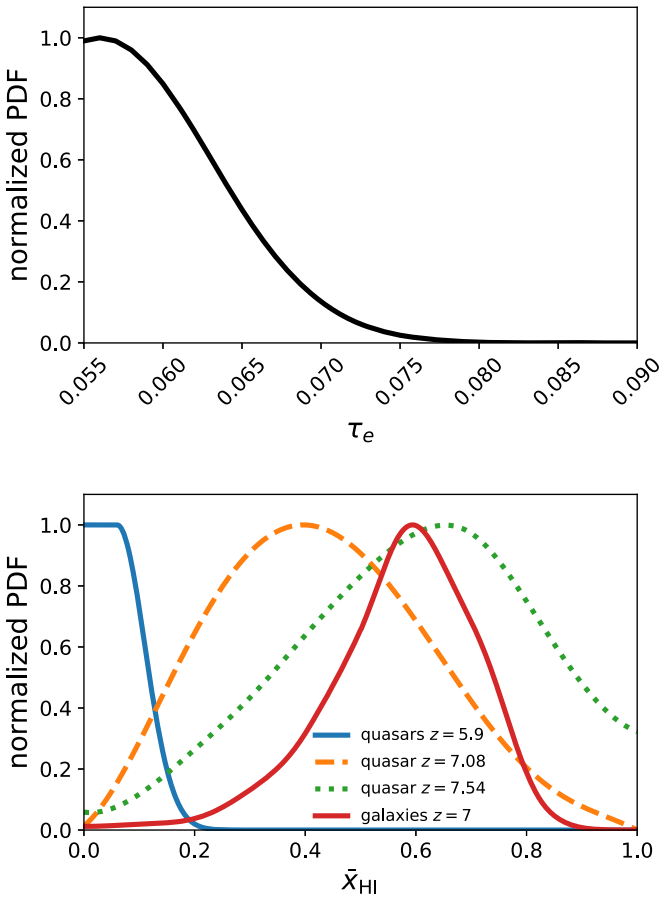

Figure 2. PDFs of the external constraints used in our combined analysis. Each PDF is normalized to its peak amplitude. Top: PDF of the electron scattering optical depth estimated by *Planck* (Planck Collaboration VI 2018). We model it as a Gaussian centered at $\tau_{\rm e} = 0.056$ and with a width $\sigma = 0.007$. Bottom: PDFs of the average neutral hydrogen fraction derived from the spectra of high-z quasars and galaxies. The PDF from the quasar at $z = 5.9$ was obtained from the fraction of dark Lyα and Lyβ pixels in the quasar spectra (McGreer et al. 2015). The PDFs from the quasars at $z = 7.08$ (Greig et al. 2017) and $z = 7.54$ (Bañados et al. 2018) were derived from the quasars' Lyα damping wings. The PDF at $z = 7$ (Mason et al. 2018) was obtained from the analysis of Lyα transmission from 68 LBGs.

During the preparation of this manuscript, Greig et al. (2019) presented a new analysis of J1342+0928 that also accounts for the sightline variance effect. Unlike Bañados et al. (2018) and Davies et al. (2018), they do not find evidence for a significantly neutral IGM at $z = 7.54$. Their best estimates for $\bar{x}_{\rm H\,I}$—which depend on the reionization morphology assumed—are below 0.3 and consistent with zero at $\lesssim 1\sigma$. However, because the $\bar{x}_{\rm H\,I}$ PDFs are wide, these results disagree with Bañados et al. (2018) and Davies et al. (2018) only at $\lesssim 1.5\sigma$. Here we use the conservative estimate from Bañados et al. (2018) and leave incorporating newer quasar constraints on $\bar{x}_{\rm H\,I}$ for future work.

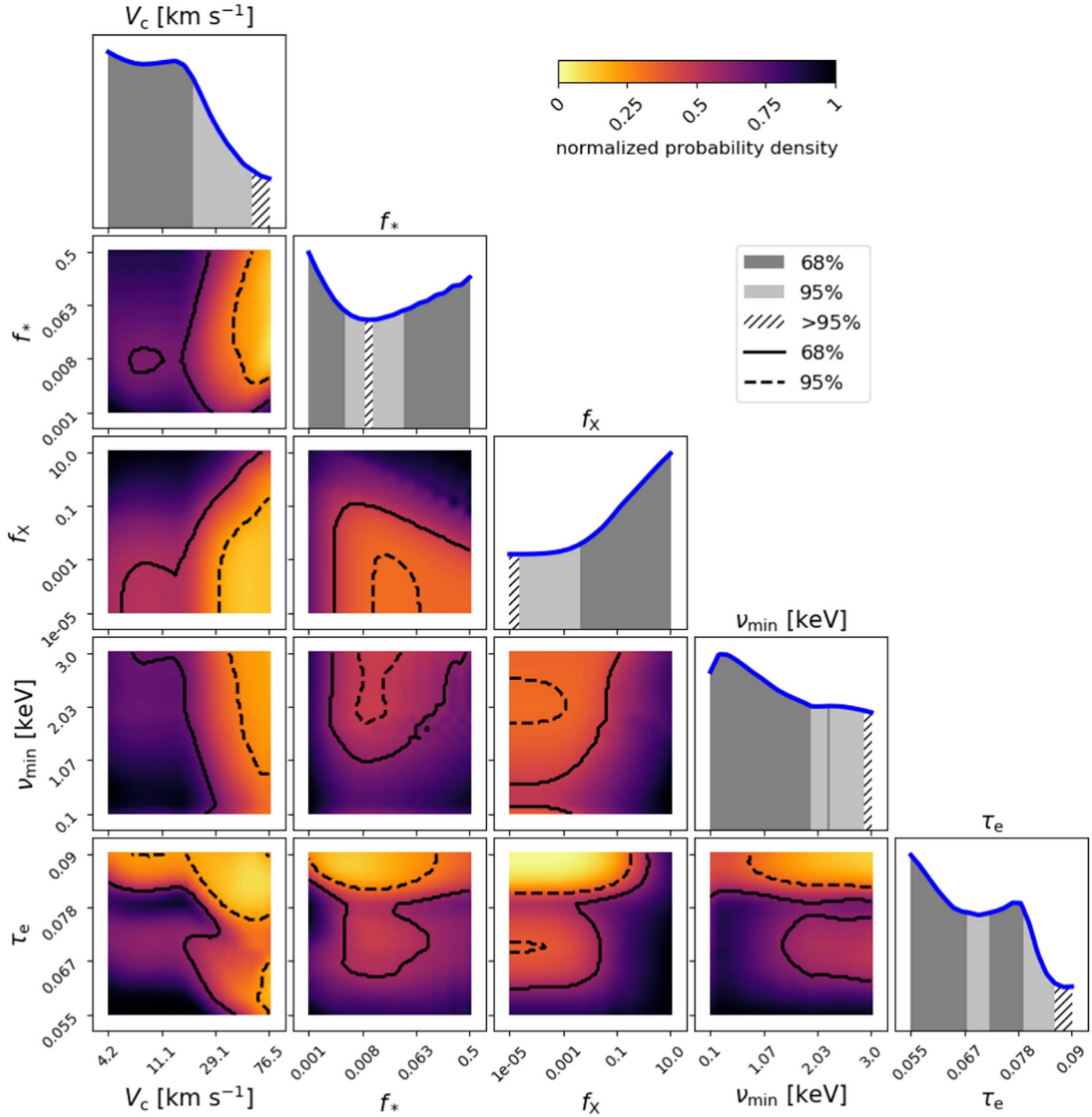

Figure 3. PDFs of the astrophysical parameters derived from the analysis of the EDGES High-Band spectrum alone (Monsalve et al. 2017b) assuming fixed $R_{mfp} = 30$ Mpc. Each PDF is normalized to its peak amplitude. The regions of parameter space that are disfavored by EDGES (depicted as hatched and light gray bands in the 1D PDFs and as yellow areas on the 2D PDFs) are those of high V_c, intermediate f_*, low f_X, high ν_{min}, and high τ_e. The marginalized 68% and 95% limits obtained from this analysis are listed in Table 2 as case A, as well as in Table 3 for τ_e.

4. Results

Now we present the constraints on the six astrophysical parameters derived from the analysis of (1) the EDGES data, (2) the external constraints from *Planck*+quasars+galaxies, and (3) the combination EDGES+*Planck*+quasars+galaxies. In particular, we show results for (2) because the external constraints have a significant impact on V_c and R_{mfp}, in addition to τ_e, and it is important to highlight these results independently. The results for the case where ν_{min} is the fifth parameter in the analysis are shown in Figures 3, 5, and 6. The results for R_{mfp} when treated as the fifth parameter are shown in Figure 7. In Figure 7 we do not show the PDFs that only involve the other four parameters because they are similar to those in Figures 3, 5 and 6. Table 2 presents the marginalized 68% and 95% limits on all the parameters from the EDGES-only and combined analyses. In Table 3 we show the estimates for τ_e derived from each individual observation, as well as for different

Table 2
Marginalized 68% and 95% Parameter Limits

Parameter	Case	68% Min	68% Max	95% Min	95% Max
V_c (km s^{-1})	A	4.2	19.3	4.2	56.0
	B	4.2	21.5	4.2	58.1
	C	6.0	11.1	4.2	52.0
		18.6	46.6		
	D	6.0	11.1	4.2	52.0
		17.9	46.6		
f_*	A	0.001	0.004	0.001	0.009
		0.039	0.5	0.012	0.5
	B	0.001	0.004	0.001	0.011
		0.036	0.5	0.015	0.5
	C	0.001	0.007	0.001	0.014
		0.062	0.5	0.019	0.5
	D	0.001	0.009	0.001	0.38
		0.036	0.045		
		0.053	0.324		
f_X	A	0.0042	10	2×10^{-5}	10
	B	0.0025	10	2×10^{-5}	10
	C	0.0021	10	2×10^{-5}	10
	D	0.0012	10	2×10^{-5}	10
ν_{min} (keV)	A	0.1	1.9	0.1	2.9
		2.2	2.3		
	C	0.1	2.0	0.1	2.9
τ_e	A	0.055	0.067	0.055	0.086
		0.072	0.080		
	B	0.055	0.072	0.055	0.087
		0.074	0.079		
	C	0.055	0.057	0.055	0.065
		0.059	0.063		
	D	0.055	0.057	0.055	0.065
		0.059	0.063		
R_{mfp} (Mpc)	B	10.0	36.1	10.0	39.1
				41.1	50.0
	D	27.5	50.0	14.3	50.0

Note. (1) Cases: (A) EDGES only, $R_{mfp} = 30$ Mpc; (B) EDGES only, $\nu_{min} = 0.5$ keV; (C) combined constraints, $R_{mfp} = 30$ Mpc; and (D) combined constraints, $\nu_{min} = 0.5$ keV. (2) For some parameters, a given probability volume (68% or 95%) is contained within two or three disjoint value ranges. These ranges are presented in the table as rows associated with the same "Case" letter.

combinations. Unless stated otherwise, the limits quoted for reference in the rest of this section correspond to the case with ν_{min} as fifth parameter.

4.1. EDGES-only Analysis

As we can see in the 1D and 2D PDFs of Figure 3 and the top row of Figure 7, the EDGES High-Band measurement provides significant discrimination across the explored parameter space. Monsalve et al. (2017b) showed that the High-Band data are incompatible with global signals that have high amplitude and vary rapidly within the band. For our models and parameterization, this translates into the disfavoring of models with high V_c, intermediate f_*, low f_X, and high τ_e. Models with high ν_{min} and high R_{mfp} are also disfavored, although the data are less sensitive to variations in these parameters due to their weaker impact on the global signal.

Table 3
Marginalized 68% Limits for τ_e

Observation	Min	Max
quasars $z = 5.9$	0.068	0.090
quasar $z = 7.08$	0.055	0.065
quasar $z = 7.54$	0.055	0.065
galaxies $z = 7$	0.055	0.061
Planck	0.055	0.063
EDGES	0.055	0.067
	0.072	0.080
quasars	0.057	0.067
quasars + galaxies	0.055	0.057
	0.059	0.064
quasars + galaxies + *Planck*	0.055	0.058
	0.059	0.063
quasars + galaxies + *Planck* + EDGES	0.055	0.057
	0.059	0.063

Note. (1) The τ_e range explored is 0.055–0.090. As the combined constraints prefer low τ_e, with high probability at ≈0.055, we plan to extend the range below 0.055 in future versions of `Global21cm`. (2) These constraints are for $R_{mfp} = 30$ Mpc. The largest difference in the τ_e limits when fixing instead $\nu_{min} = 0.5$ keV occur when using EDGES data only. These two results are shown as cases A and B in Table 2. For the other observations or combinations, the difference in the τ_e limits between $R_{mfp} = 30$ Mpc and $\nu_{min} = 0.5$ keV is $\lesssim 10^{-3}$. (3) In some cases, the 68% probability volume is contained within two disjoint value ranges. These ranges are presented as two rows.

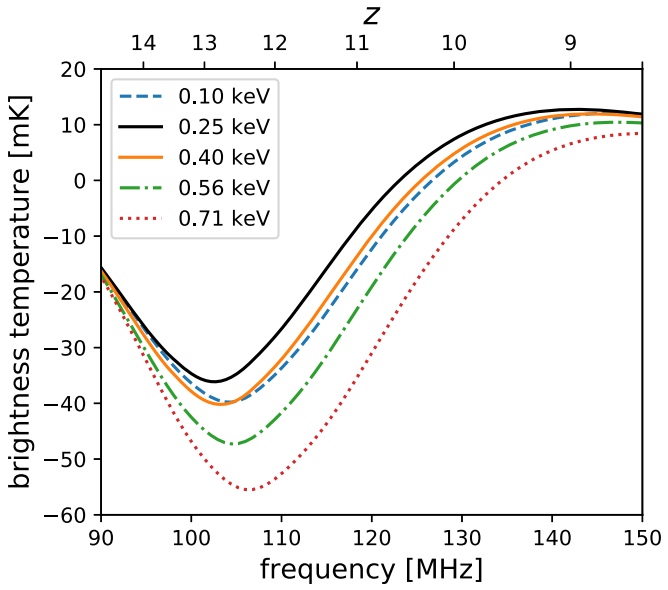

Figure 4. Variation of the global signal for low values of ν_{min}. Over most of the parameter range explored in this paper, as ν_{min} decreases, the absorption amplitude also decreases and the absorption peak is shifted to lower frequencies. However, this trend is reversed below $\nu_{min} \approx 0.25$ keV, as shown in this figure. The signals shown here as examples correspond to $V_c = 76.5$ km s^{-1}, $f_* = 0.026$, $f_X = 10$, $\tau_e = 0.06$, and $R_{mfp} = 31$ Mpc.

From the PDFs, we derive the following constraints on each one of the parameters:

V_c: Along with f_*, V_c determines the timing of the Lyα coupling and drives the evolution of the signal all the way to the onset of heating, affecting the location and depth of the absorption trough. As Cohen et al. (2017) and A. Cohen et al. (2019, in preparation) indicate (e.g., Figure 6 of the latter paper), Lyα coupling is predicted to take place at $z \gtrsim 20$ and therefore cannot be directly probed by EDGES High-Band.

However, the High-Band data are sensitive to the features of the absorption and this enables us to assign probabilities to the models as a function V_c. As we see in the PDFs, high values of V_c (i.e., higher minimum mass of star-forming haloes) are disfavored because they result in narrower troughs centered at higher frequencies, to which EDGES has higher sensitivity. We rule out $V_c > 19.3\,\mathrm{km\,s^{-1}}$ at 68% confidence. This velocity threshold is close to the limit of atomic cooling and corresponds to the minimum halo mass of $1.3 \times 10^8\,M_\odot$ at $z = 10$. At 95% confidence we rule out $V_c > 56\,\mathrm{km\,s^{-1}}$, which corresponds to $M_{\mathrm{min}} \sim 3.1 \times 10^9\,M_\odot$ at $z = 10$.

f_*: Low values of f_* result in inefficient Lyα coupling, and as a result, shallow absorption profiles, while high values produce deeper but wider absorption profiles. The EDGES High-Band data and modeling provide low sensitivity to both types of signals, which results in a high probability assigned to low and high f_*. On the other hand, our analysis disfavors intermediate values of f_*, which produce sharper signatures in the High-Band range. Specifically, we rule out $0.4\% < f_* < 3.9\%$ (68%).

f_X: The X-ray heating efficiency is one of the parameters that control the location of the absorption minimum and the high-frequency slope of the trough. A higher f_X results in sharper but shallower troughs centered at lower frequencies owing to more efficient heating, and could also result in a significant emission feature during reionization. A lower f_X produces deeper and wider troughs centered at higher frequencies, as well as a suppressed or vanishing emission signal. The EDGES spectrum is more sensitive to low-f_X signals, although the high sensitivity expected from their large depth is compensated by the lower sensitivity due to the larger width. As we can see in the PDFs, low values of f_X are disfavored for most of the parameter combinations. After marginalization, we rule out $f_X < 0.0042$ (2×10^{-5}) at 68% (95%) confidence.

ν_{min}: Although the global signal is less sensitive to changes in ν_{min} than to changes in the previous parameters, this sensitivity is enough for EDGES High-Band to star placing initial constraints. Specifically, EDGES disfavors high values of ν_{min}, corresponding to harder X-ray SEDs that produce wider and deeper absorption troughs shifted to higher frequencies. As ν_{min} decreases, the fraction of soft X-rays emitted by sources increases, which results in more efficient IGM heating and in earlier and shallower absorption troughs. Our conservative 68% upper limit is $\nu_{\mathrm{min}} = 2.3$ keV; however, as can be seen in the 1D ν_{min} PDF and in Table 2, this limit accounts for the narrow range 2.2–2.3 keV that also falls within the 68% limits. Ignoring this range, we obtain the limit $\nu_{\mathrm{min}} = 1.9$ keV (68%). In the 1D PDF we also notice that the probability has a peak at $\nu_{\mathrm{min}} \approx 0.25$ keV and that it decreases for lower values. We explore the origin of this feature in Figure 4; we see that for $\nu_{\mathrm{min}} > 0.25$ keV, and as ν_{min} decreases, the absorption trough in the 21 cm signal becomes shallower and the center is shifted to lower frequencies. However, as values reach and decrease below $\nu_{\mathrm{min}} \approx 0.25$ keV, the absorption becomes deeper again and the center is shifted to higher frequencies, approaching the shapes observed for $\nu_{\mathrm{min}} > 0.25$ keV. This reversed dependence of the global signal below a ν_{min} threshold is due to an effective hardening of the X-ray SED at low ν_{min}, as most of the energy produced by the sources is deposited very close to the star-forming regions (see Section 2.2.5 of Greig & Mesinger 2017b). The 1D ν_{min} PDF reflects that EDGES High-Band has the lowest constraining capability around this threshold.

τ_e: Changes in τ_e affect the evolution of the IGM ionized hydrogen fraction. Higher values imply higher ionizing efficiency of sources, which leads to an earlier reionization and a global signal with a shallower but narrower absorption feature and a weaker emission peak. Lower values of τ_e result in delayed, deeper, and wider troughs, as well as in a potentially stronger emission feature that peaks at higher frequencies. The general trend in the τ_e PDFs from EDGES is a probability density that decreases for higher τ_e, which is consistent with the preference of low τ_e by *Planck*. Our conservative 68% upper limit, accounting for the high-probability bump centered at $\tau_e \approx 0.076$ (described in the next paragraph), is $\tau_e = 0.080$. We note, however, that due to the higher noise at the low end of the spectrum ($\lesssim$110 MHz), the sensitivity of the EDGES High-Band data to models with $\tau_e \gtrsim 0.09$ decreases significantly. Higher-sensitivity measurements at $\lesssim$110 MHz, such as those provided by EDGES Low-Band, are required to access these higher optical depths.

Beyond the main trend, in Figures 3 and 7 (top row) we see that the τ_e PDFs have the most irregular structure among the parameters. When projected onto the 1D τ_e PDF, this structure is seen as a bump at $\tau_e \approx 0.076$. To understand its origin, we compute the PDFs for simulated EDGES spectra. These spectra are produced starting from the five-term foreground model that best fits the measured spectrum, to which we add noise drawn from the same noise profile as the measurement. We also add ripples that mimic those observed in the measured spectrum above the foreground model (see Figure 4 of Monsalve et al. 2017b). In some cases we add ripples only within sub-bands of the spectrum in order to evaluate their specific effect. We find that the bump at $\tau_e \approx 0.076$ is produced by 21 cm signals that match ripples in the measured spectrum within the range ≈125–145 MHz. Simulations without these ripples produce PDFs that decrease smoothly with τ_e, without a bump at ≈0.076. Future reprocessing and modeling of the High-Band data might reveal the origin of the ripples. New measurements with different instruments could be used to revise the PDFs of this parameter. As seen in the 1D PDF of Figure 3, the bump at $\tau_e \approx 0.076$ represents a second range contained within the 68% confidence limits, in addition to the larger range at low τ_e. Ignoring the bump and considering only the low τ_e region, the 68% limit is $\tau_e = 0.067$.

R_{mfp}: The sensitivity of the global signal to changes in R_{mfp} is lower than for the other parameters and comparable to that for ν_{min}. Higher values of R_{mfp} correspond to a faster growth of ionized bubbles, and thus to a faster reionization process and a sharper end of reionization (Greig & Mesinger 2017a, 2017b). The 1D R_{mfp} PDF in the top row of Figure 7 shows that the EDGES spectrum disfavors higher values of R_{mfp}. We rule out $R_{\mathrm{mfp}} > 36$ Mpc (68%) for fixed $\nu_{\mathrm{min}} = 0.5$ keV.

In Table 2 the constraints from the EDGES-only analyses are presented as cases A (for fixed $R_{\mathrm{mfp}} = 30$ Mpc) and B (for fixed $\nu_{\mathrm{min}} = 0.5$ keV).

4.2. External Constraints

Here we describe the constraints on the astrophysical parameters derived from the τ_e estimate from *Planck*, the $\bar{x}_{\mathrm{H\,I}}$ estimates from quasars at $z = 5.9$, 7.08, and 7.54, and the $\bar{x}_{\mathrm{H\,I}}$ estimate from galaxies at $z = 7$. These external estimates characterize the evolution of the neutral hydrogen fraction and

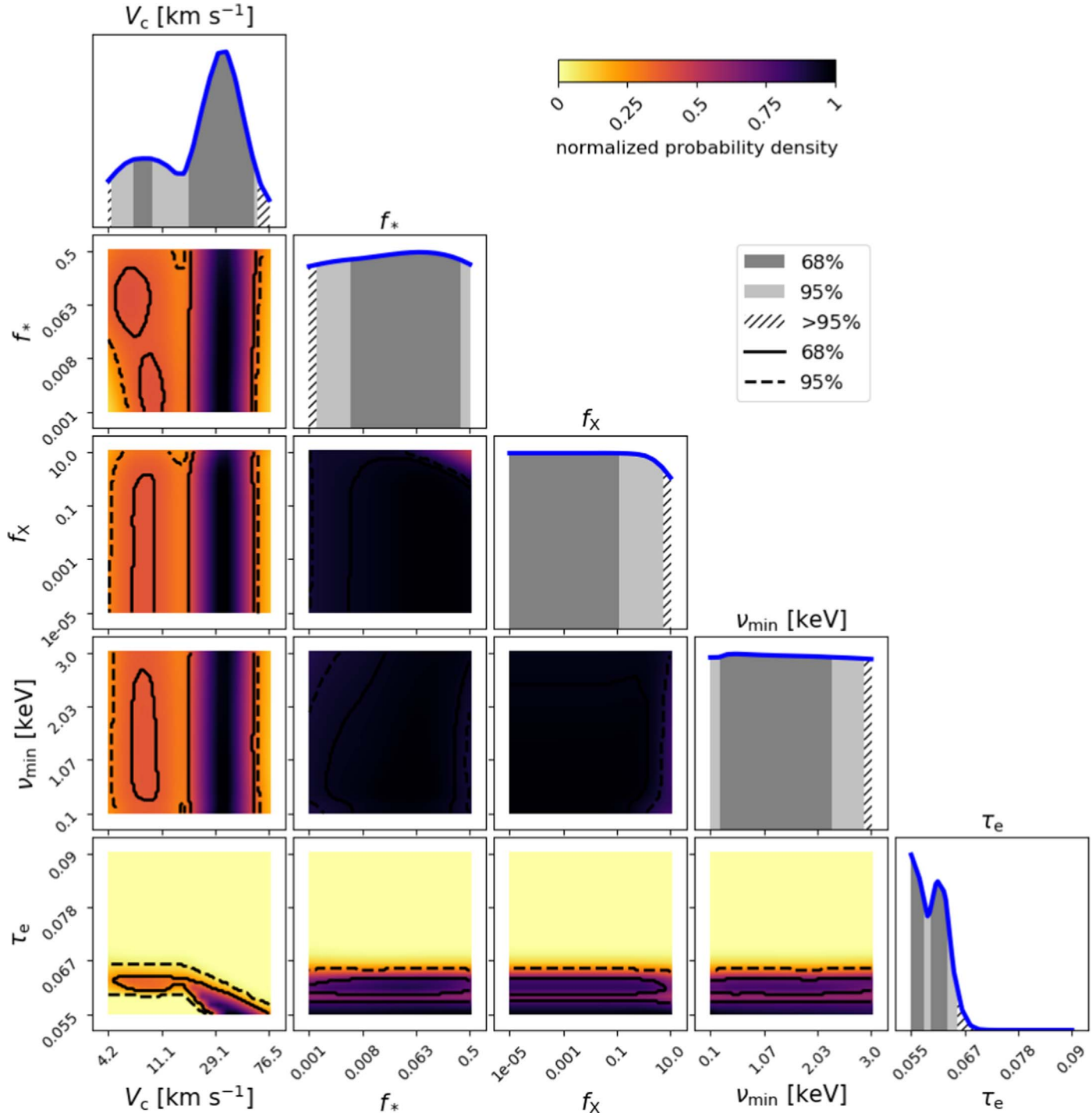

Figure 5. PDFs of the astrophysical parameters derived from the analysis of the external constraints alone and assuming fixed $R_{\rm mfp} = 30$ Mpc. Each PDF is normalized to its peak amplitude. The external constraints correspond to a prior on τ_e from *Planck* (Planck Collaboration VI 2018) and estimates for $\bar{x}_{\rm H\,I}$ from high-z quasars (McGreer et al. 2015; Greig et al. 2017; Bañados et al. 2018) and LBGs (Mason et al. 2018). The external constraints are described in Section 3.2 and depicted in Figure 2. An important result of this analysis is the strong joint constraint on $\tau_e - V_c$. The marginalized results for τ_e are summarized in Table 3.

therefore strongly constrain the reionization parameters, i.e., τ_e and $R_{\rm mfp}$. However, due to the correlation between reionization, the star formation history, and—to a lesser degree—heating, there is some degeneracy between the reionization parameters and V_c, as well as a much weaker degeneracy with f_*, f_X, and $\nu_{\rm min}$. As we show in this section, these degeneracies are reflected in the parameter constraints. The results of the analyses that combine all the external estimates are presented in Figure 5 and in the middle row of Figure 7.

Consider first the limits from the external estimates on τ_e, summarized in Table 3. The upper limit $\bar{x}_{\rm H\,I} \leqslant 0.06 + 0.05$ (68%) at $z = 5.9$ from McGreer et al. (2015) significantly reduces the probability of late reionization and therefore of low τ_e. From this constraint alone we derive the marginalized lower limit $\tau_e > 0.068$ (0.056) at 68% (99%) confidence. On the other hand, quasars at $z \gtrsim 7$ suggest that the IGM was significantly neutral at these redshifts, with $\bar{x}_{\rm H\,I} = 0.40^{+0.21}_{-0.19}$ (68%, Greig et al. 2017) and $\bar{x}_{\rm H\,I} = 0.65^{+0.15}_{-0.32}$ (68%, Bañados

et al. 2018) measured at $z = 7.08$ and $z = 7.54$, respectively. These data complement the upper limit from McGreer et al. (2015) by disfavoring an early reionization and thus high values of τ_e. Specifically, both measurements independently impose the upper limit $\tau_e < 0.065$ (68%). Finally, the tighter constraint $\bar{x}_{\rm H\,I} = 0.59^{+0.11}_{-0.15}$ (68%) from LBGs at $z = 7$ gives preference to lower optical depths than the quasars. Analyzing this constraint alone results in the upper limit $\tau_e < 0.061$ (68%), which we note mildly disagrees with the lower limit from McGreer et al. (2015).

Joint analysis of the three quasar constraints favors τ_e in the range 0.057–0.067 (68%). This range is tighter than current estimates from *Planck* and in mild disagreement with them ($\lesssim 2\sigma$, depending on the specific estimate) because the *Planck* best fits lie below our quasar 68% range (Planck Collaboration VI 2018). Combining the quasar and LBG neutral fraction constraints we obtain the upper limit $\tau_e < 0.064$ (68%). Here, the tight neutral fraction constraint from LBGs has increased the consistency between this combined τ_e result and the τ_e estimates from *Planck*. This is noteworthy considering that the assumed ionization histories are different; *Planck* uses a "tanh" phenomenological dependence of $\bar{x}_{\rm H\,I}$ on redshift, while we used the realistic neutral fractions produced by `Global21cm` to derive the quasar and LBG constraints. Finally, incorporating the *Planck* prior ($\tau_e = 0.056 \pm 0.007$), we obtain $\tau_e < 0.063$ (68%). This latter result, derived from the combination of our five external constraints, is the one corresponding to the 1D PDF of Figure 5. In this PDF we see a probability dip in the middle of an otherwise smooth trend of increasing probability toward low values. The dip has the effect of excluding the narrow range $\tau_e = 0.058$–0.059 from the 68% probability region. This feature is explained by the combination of two factors: (1) as we pointed out above, the lower values of τ_e favored by LBGs (and *Planck*) are in mild conflict with the higher τ_e preferred by the quasars; and (2) the piecewise dependence of the SFE on V_c, as implemented in `Global21cm`, which induces features in the PDFs (more details below). Considering that the τ_e values preferred by the combined constraints are low and reach our current low-end optical depth cutoff even when we include the upper limit on $\bar{x}_{\rm H\,I}$ from McGreer et al. (2015), we plan to extend the parameter range to values below $\tau_e = 0.055$ in future versions of `Global21cm`.

The joint constraints on τ_e and V_c obtained when we apply all the external estimates are shown in the corresponding 2D PDF of Figure 5. This PDF reflects the degeneracy between these two parameters in their effect on the global reionization history. For a fixed τ_e, reionization is slower in the case of low V_c. In particular, for low V_c the tail of $\bar{x}_{\rm H\,I}$ at the end of reionization is longer, and therefore the values of $\bar{x}_{\rm H\,I}$ at a fixed redshift are higher than in the case of higher V_c. Hence, for low τ_e the scenarios with lower V_c are more likely to violate the upper limit on $\bar{x}_{\rm H\,I}$ at $z = 5.9$. On the other hand, to keep a sufficiently high $\bar{x}_{\rm H\,I}$ as required at $z \gtrsim 7$, the constraints on the neutral fraction prefer low V_c at low τ_e. As a result, the high-probability region in the $\tau_e - V_c$ 2D PDF is confined to a narrow band that is mainly produced by the complementary effects of the $\bar{x}_{\rm H\,I}$ constraint at $z = 5.9$ and those at $z \gtrsim 7$. At $V_c < 16.5\,{\rm km\,s^{-1}}$, the band is centered at $\tau_e \approx 0.064$ and only has a weak dependence on V_c. At $V_c = 16.5\,{\rm km\,s^{-1}}$ the band goes through a knee, and for higher V_c, τ_e decreases for increasing V_c. Because the *Planck* prior and the $\bar{x}_{\rm H\,I}$ estimate from LBGs prefer lower τ_e, the highest probability along the band occurs for high V_c. The sharpness of the knee is not physical; it is an artifact of our models produced by the piecewise SFE of Equation (2), which changes the trend exactly at $V_c = 16.5\,{\rm km\,s^{-1}}$, corresponding to the atomic cooling threshold. We observe that after marginalization, the knee results in relatively sharp features in the 1D PDFs of V_c and τ_e; specifically, probability dips at $V_c \approx 16.5\,{\rm km\,s^{-1}}$ and $\tau_e \approx 0.058$. We plan to improve the V_c transition in future modeling.

In the 1D V_c PDF it is more evident that unlike the EDGES data, the external constraints prefer high values of V_c. This PDF is dominated by a bump that contains most of the 68% probability volume and peaks at $V_c \approx 35\,{\rm km\,s^{-1}}$. The 68% lower limit of the bump is $V_c = 17.9\,{\rm km\,s^{-1}}$, i.e., close to the atomic cooling threshold, and the upper limit is $58.1\,{\rm km\,s^{-1}}$, which corresponds to $M_{\rm min} \sim 3.5 \times 10^9\,M_\odot$ at $z = 10$.

At fixed τ_e and V_c, the 2D PDFs of f_*, f_X, and $\nu_{\rm min}$ are nearly flat, reflecting the small effect of these parameters on $\bar{x}_{\rm H\,I}$. The contribution of X-rays to reionization is non-negligible, however. This can be appreciated better after marginalization, as a mild preference of the data for high f_*, low f_X, and low $\nu_{\rm min}$, in their 1D PDFs.

As the middle row of Figure 7 shows, the external constraints favor high values of $R_{\rm mfp}$, which (like high V_c) correspond to a faster reionization. This is opposite to the preference by EDGES data and results from the need to simultaneously satisfy the neutral fraction upper limit at $z = 5.9$ and the high neutral fraction at $z \gtrsim 7$, as well as produce a low optical depth.

4.3. Combined Analysis

Next, we present the astrophysical constraints obtained in the analysis that includes the EDGES High-Band data and the external estimates for the optical depth and the neutral hydrogen fraction. Compared to the results from EDGES alone, the external estimates have the strongest impact on the PDFs of τ_e, V_c, and $R_{\rm mfp}$, while the PDFs of f_*, f_X, and $\nu_{\rm min}$ are mainly determined by EDGES. The results are shown in Figure 6 (for fixed $R_{\rm mfp} = 30$ Mpc) and in the bottom row of Figure 7 (for fixed $\nu_{\rm min} = 0.5$ keV). They are also summarized in Table 2 (as cases C and D) and in Table 3 for τ_e.

Considering the 2D PDF for τ_e and V_c in Figure 6, we see that the narrow high-probability band at low τ_e, produced by the external constraints and introduced in Section 4.2, remains as the main feature. Compared to the result from the external constraints alone, in the combined analysis the EDGES data have the effect of reducing the probability at high V_c. This is seen more clearly in the 1D V_c PDF, where we also note that EDGES produces higher probabilities at lower V_c; in particular, the region of low V_c contained within the 68% probability volume is wider in the case of the combined constraints. From this PDF, we disfavor at 68% confidence $V_c < 6.0\,{\rm km\,s^{-1}}$ and $V_c > 46.6\,{\rm km\,s^{-1}}$; this corresponds to $M_{\rm min} < 3.9 \times 10^6\,M_\odot$ and $M_{\rm min} > 1.8 \times 10^9\,M_\odot$ at $z = 10$. We note that a range of values around the dip at $V_c = 16.5\,{\rm km\,s^{-1}}$ (the atomic cooling threshold) is also outside the 68% probability region. At 95% confidence we derive the upper limit $V_c = 52\,{\rm km\,s^{-1}}$, equivalent to $2.5 \times 10^9\,M_\odot$ at $z = 10$.

The combined constraint on τ_e is driven by *Planck* + quasars + galaxies, with EDGES having a marginal contribution. Specifically, when we combine EDGES and the external

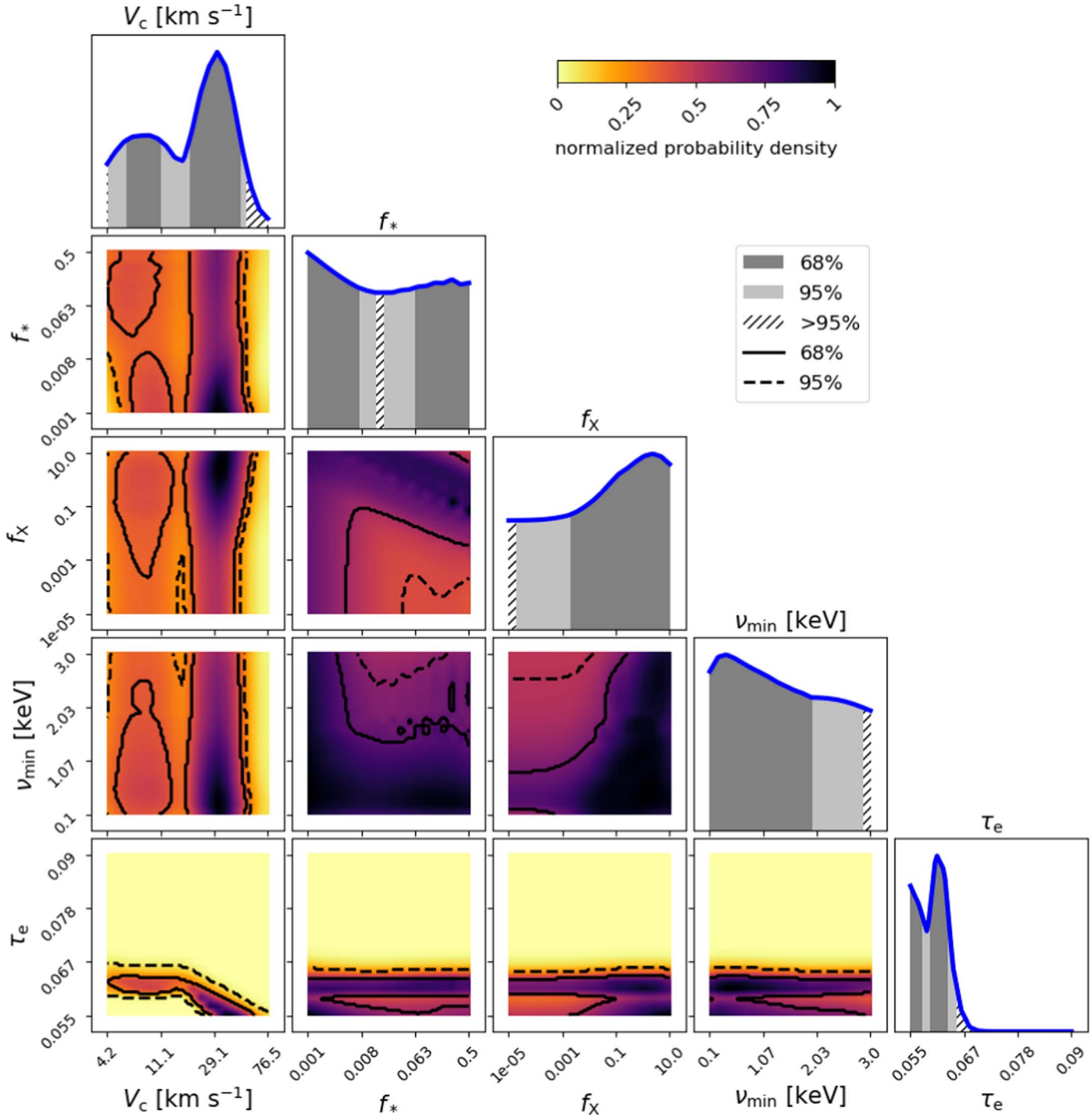

Figure 6. PDFs of the astrophysical parameters derived from the combined analysis that includes the EDGES High-Band spectrum (Monsalve et al. 2017b) and external estimates for τ_e and $\bar{x}_{H\,I}$ (McGreer et al. 2015; Greig et al. 2017; Bañados et al. 2018; Mason et al. 2018; Planck Collaboration VI 2018). Here we assume a fixed $R_{mfp} = 30$ Mpc. Each PDF is normalized to its peak amplitude. Comparing the 1D PDFs in this figure with those in Figures 3 and 5, we see that (1) EDGES drives the constraints on f_*, f_X, and ν_{min}, (2) the external observations drive the constraint on τ_e, and (3) EDGES and the external observations impact significantly the constraint on V_c. The marginalized 68% and 95% limits from this analysis are listed in Table 2 as case C, as well as in Table 3 for τ_e.

observations, we obtain the upper limit $\tau_e < 0.063$ at 68% confidence, with the narrow range $\tau_e = 0.057$–0.059 outside the 68% limits. This is almost identical to the result for *Planck* + quasars + galaxies alone. It nonetheless reflects a broad consistency between EDGES and the external observations.

The shapes of the f_*, f_X, and ν_{min} 1D PDFs derived from the combined analysis are very close to those found using EDGES alone. As an example of the minor changes in the limits, the 68% lower limit on f_X decreases from 0.0042 for EDGES alone to 0.0021 in the combined analysis, which can be explained by the small decrease in the probability of high f_X produced by the external constraints on reionization.

Finally, and as for τ_e, the combined constraint on R_{mfp} is mainly determined by the external observations. Comparing the 1D PDFs of R_{mfp} in Figure 7, we see that the PDF derived from the combined analysis (bottom row) is very similar to that

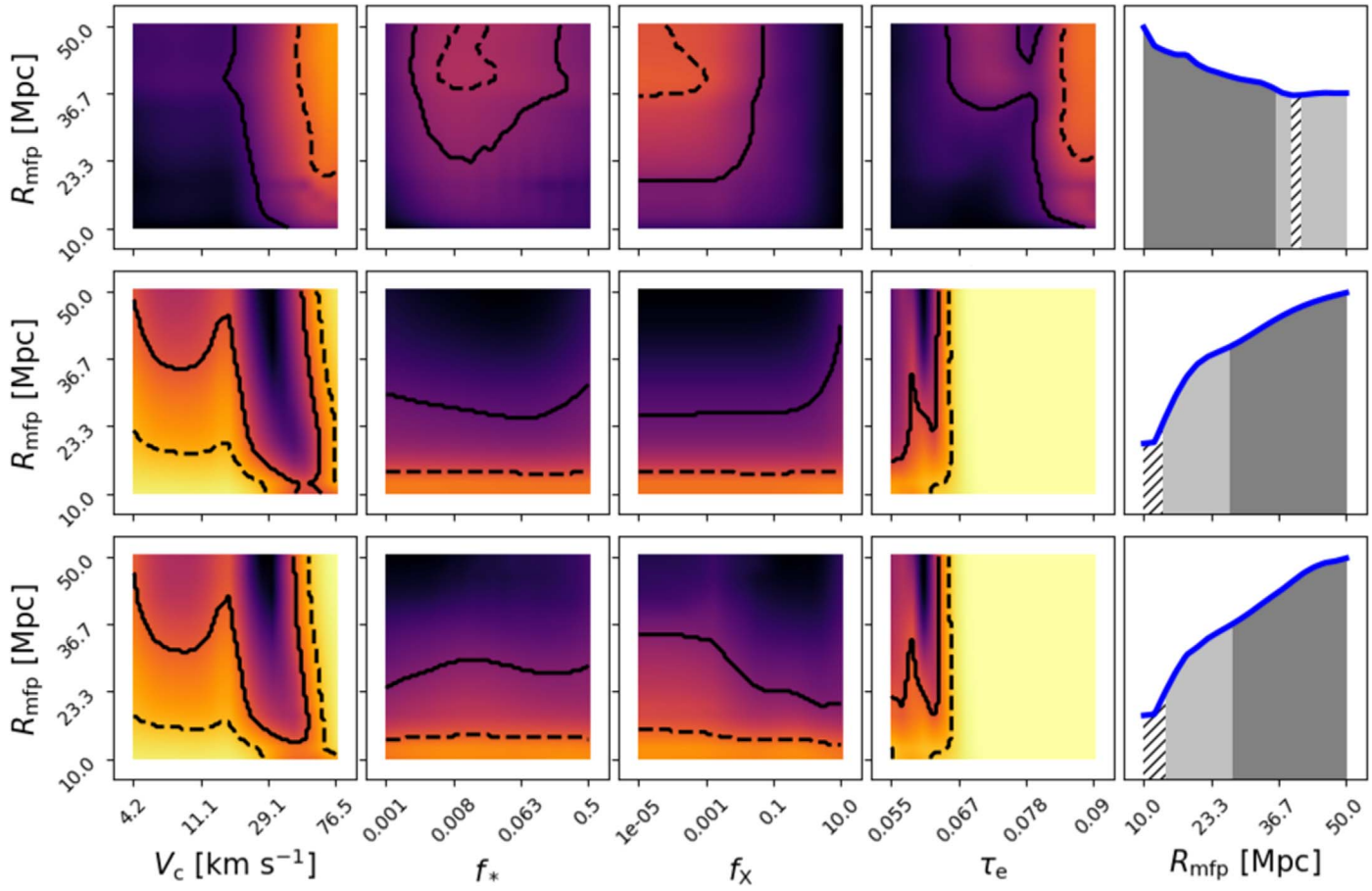

Figure 7. PDFs of R_{mfp} derived from the analysis of (top row) the EDGES High-Band spectrum (Monsalve et al. 2017b), (middle row) the external estimates for τ_e and $\bar{x}_{H\,I}$, from *Planck* and high-z quasars and galaxies (McGreer et al. 2015; Greig et al. 2017; Bañados et al. 2018; Mason et al. 2018; Planck Collaboration VI 2018), and (bottom row) the combination EDGES + *Planck* + quasars + galaxies. For these results we have fixed $\nu_{min} = 0.5$ keV. Each PDF is normalized to its peak amplitude. The color map is the same as in Figures 3, 5, and 6. In the 2D PDFs, the solid (dashed) black lines represent the 68% (95%) probability limits. The EDGES data alone disfavor high values of R_{mfp} (top row, rightmost column), which correspond to global signals with sharper features. The external constraints favor high values of R_{mfp} (middle row, rightmost column). When all the observations are combined, the external constraints have the strongest influence, and high values of R_{mfp} remain preferred (bottom row, rightmost column).

obtained from the external observations alone (middle row). Although the EDGES data disfavor high values of R_{mfp} (top row), corresponding to sharper global signals, the combined analysis prefers high R_{mfp} and yields the lower limit $R_{mfp} > 27.5$ Mpc at 68% confidence for fixed $\nu_{min} = 0.5$ keV.

5. Discussion

5.1. Parameter Degeneracy

As discussed in Section 4.2, the parameters in our analysis that drive the evolution of the neutral hydrogen fraction are τ_e and V_c, which suffer from a degeneracy in their effect on reionization.

Another example of degeneracy involves the parameters that have an effect on cosmic heating. The global 21 cm signal is sensitive to the total energy injected into the gas, which depends on several quantities, such as the SFE and the SED of X-rays (including its shape and normalization). In our parameterization, the total number of X-ray photons that contribute to heating is determined by the values of V_c, f_*, f_X, ν_{min}, and α. As a result, there are clear correlations between these parameters, which manifest themselves in the EDGES-only analysis (Figure 3) as diagonal trends on the 2D PDFs of $f_X - V_c, f_X - f_*$, (and more weakly) $\nu_{min} - V_c, \nu_{min} - f_*$, and $\nu_{min} - f_X$. The correlations demonstrate that via X-ray heating, models with high f_X and high V_c have a signature within the EDGES band that is similar to cases with low f_X and low V_c. The diagonal trend on the $f_X - f_*$ 2D PDF reflects that in the context of the global signal, the important parameter is $f_* f_X$. This degeneracy is broken only for very low values of f_*, for which Lyα coupling is inefficient. Finally, the degeneracy on the $\nu_{min} - f_X$ plane reflects that hard spectra (high ν_{min}) generate less heating and require higher f_X to produce absorption troughs similar to models with low values of the two parameters.

The existing degeneracies in the global signal analysis arise because the parameterization of the 3D simulations used to train `Global21cm` is not optimized to represent the global signal alone, but instead to track the temporal evolution of the 21 cm signal within a large cosmological volume from which higher-order statistics, such as power spectra, can also be computed. In the future, an additional tool could be developed to establish consistency between the constraints obtained from radiometric and interferometric measurements, and reduce the degeneracies. Another important remaining task corresponds to finding a set of independent parameters to describe and constrain the astrophysics of the early universe via the global 21 cm signal alone. We leave this to future work.

5.2. Comparison with Previous Results

In this paper we constrain astrophysical processes during cosmic dawn and reionization, i.e., the same periods that were constrained by Greig & Mesinger (2017a) and M18. However, as pointed out in Section 1, in these works the astrophysical models were generated using the `21cmFAST` code, which differs from `Global21cm` in details of the processes that are modeled (e.g., Visbal et al. 2012; Fialkov et al. 2013; Cohen et al. 2016). Other differences include different parameterization and parameter ranges explored, as well as the parameters that were kept fixed during the exploration of the parameter space. These differences in modeling prevent us from making a quantitative comparison. The comparison is made even more difficult by the use of different external constraints. Therefore we here limit ourselves to a high-level comparison and leave more detailed discussions for future work.

Greig & Mesinger (2017a) explored parameters relevant to reionization—ζ, $T_{\rm vir}^{\rm min}$, and $R_{\rm mfp}$—assuming saturated X-ray heating and a SFE of 5%. They found that the $\tau_{\rm e}$ estimate from *Planck* 2016 and the $\bar{x}_{\rm H\,I}$ quasar constraints restrict the high-probability range in the joint $\zeta - T_{\rm vir}^{\rm min}$ PDF to a relatively narrow band across the plane (see the bottom row of their Figure 8). Although this is a significant result, the band indicates a strong degeneracy between these parameters that prevents tight 1D marginalized constraints, in particular on ζ. In M18 we found that combining the EDGES High-Band data with the *Planck* 2016 + quasar constraints slightly decreased the degeneracy between $T_{\rm vir}^{\rm min}$ and ζ by reducing the probability of high $T_{\rm vir}^{\rm min}$ and high ζ. We also incorporated into the analysis the X-ray heating parameters $L_{\rm X<2\,keV}/{\rm SFR}$ and E_0, originally introduced in Greig & Mesinger (2017b). The SFE was still kept at 5%. We obtained the following 68% marginalized limits: (1) $5 < \log_{10}(T_{\rm vir}^{\rm min}/{\rm K}) < 5.6$, (2) $10 < \zeta < 148.4$, and (3) $0.62 < E_0/{\rm keV} < 1.5$. We also found that the 68% confidence region of the soft-band X-ray luminosity was restricted to two ranges: $38 < \log_{10}(L_{\rm X<2\,keV}/{\rm SFR}/{\rm erg\ yr\ s^{-1}}\,M_\odot^{-1}) < 39$ and $40.8 < \log_{10}(L_{\rm X<2\,keV}/{\rm SFR}/{\rm erg\ yr\ s^{-1}}\,M_\odot^{-1}) < 42$.

The most direct comparison between the results of this paper and those in Greig & Mesinger (2017a) and M18 corresponds to the constraints on $V_{\rm c}$ reported here and their limits on $T_{\rm vir}^{\rm min}$. These two parameters directly depend on the mass of dark matter halos and are related via (Barkana & Loeb 2001)

$$V_{\rm c} = 23.4\sqrt{\left(\frac{0.6}{\mu}\right)\left(\frac{T_{\rm vir}^{\rm min}}{1.98\times10^4}\right)}\ \ {\rm km\ s^{-1}}, \tag{6}$$

where μ is the mean molecular weight, which varies between 0.59 for a fully ionized and 1.22 for neutral primordial gas. Qualitatively, the shape of the $V_{\rm c}$ and $T_{\rm vir}^{\rm min}$ 1D PDFs is similar: in the EDGES-only case the probability increases toward lower values, while in the combined analysis a peak occurs at intermediate values. Despite this qualitative agreement, quantitatively, the constraints differ due to a number of discrepancies. The low-end cutoff in M18 is $T_{\rm vir}^{\rm min} = 10^4$ K, which corresponds to $V_{\rm c} = 16.5\,{\rm km\,s^{-1}}$ (assuming $\mu = 0.59$). This means that molecular cooling halos are not accounted for in M18. Moreover, the large high-end cutoff in M18, $T_{\rm vir}^{\rm min} = 10^6$ K, weights the probability toward higher values. This upper limit corresponds to $V_{\rm c} = 166\,{\rm km\,s^{-1}}$, i.e., $M_{\rm min} \sim 8.2\times10^{10}\,M_\odot$ at $z = 10$, while the upper limit in this paper is $76.5\,{\rm km\,s^{-1}}$, corresponding to $M_{\rm min} \sim 8.0\times10^9\,M_\odot$ at $z = 10$. The 95% combined constraint on $T_{\rm vir}^{\rm min}$ derived in M18 implies $29.6 < V_{\rm c} < 117.6\,{\rm km\,s^{-1}}$, which corresponds to $4.6\times10^8 < M_{\rm min} < 2.9\times10^{10}\,M_\odot$ at $z = 10$; while our analysis here requires $V_{\rm c} < 52\,{\rm km\,s^{-1}}$, or $M_{\rm min} < 2.5\times10^9\,M_\odot$ at $z = 10$. Inclusion of small halos with $4.2 < V_{\rm c} < 16.5\,{\rm km\,s^{-1}}$ in this work prevents us from determining a strong lower limit on $V_{\rm c}$. We note that abundance matching techniques applied to the observed luminosity function of galaxies at $z > 6$ suggest that star-forming halos of $\sim10^{10}\,M_\odot$ and lower exist at high redshifts, which disfavors values of $T_{\rm vir}^{\rm min}$ higher than 10^5 K (e.g., Mashian et al. 2016; Mirocha et al. 2017).

A direct comparison between $V_{\rm c}$ in this work and $T_{\rm vir}^{\rm min}$ in M18 is not straightforward because M18 assumed a fixed $f_* = 5\%$, while here we vary f_* over 0.1%–50%. The effect of f_* on the PDFs of $V_{\rm c}$ and $T_{\rm vir}^{\rm min}$ is as follows: for f_* much lower than 5% and all the other parameters fixed, ζ would be lower, making reionization slower and increasing the neutral fraction at a given redshift. This means that we would need to decrease $V_{\rm c}$ and $T_{\rm vir}^{\rm min}$ in order to produce more ionizing photons and compensate for the lower ζ when fitting to the $\bar{x}_{\rm H\,I}$ constraint at $z = 5.9$. In other words, the $z = 5.9$ constraint would prefer lower values of $V_{\rm c}$ and $T_{\rm vir}^{\rm min}$, in broad agreement to what we see in our analysis when compared to M18. Increasing f_* while leaving the other parameters fixed leads to a faster reionization, which is more consistent with the constraint at $z = 5.9$.

Comparing the constraints on the ionization parameters in Greig & Mesinger (2017a), M18, and this work is also non-trivial as $\tau_{\rm e}$, which we choose to constrain instead of ζ, is an integrated quantity. A. Cohen et al. (2019, in preparation) checked that in `Global21cm`, when the *Planck* prior on $\tau_{\rm e}$ is applied, the allowed ζ is a growing function of $V_{\rm c}$ for $V_{\rm c} > 16.5\,{\rm km\,s^{-1}}$, in agreement with M18. For lower values of $V_{\rm c}$, ζ is nearly constant due to the effect of feedback mechanisms. In `Global21cm`, ζ is also a function of the SFE, which here we vary via f_* while in M18 it is kept constant. Therefore, here we expect a larger scatter in ζ at a given $V_{\rm c}$. Despite the differences in models and analyses, a high-level consistency between Greig & Mesinger (2017a), M18, and this paper, is observed in the form of the narrow high-probability bands on the $\zeta - T_{\rm vir}^{\rm min}$ and $\tau_{\rm e} - V_{\rm c}$ 2D PDFs, which are obtained when applying the external $\tau_{\rm e}$ and $\bar{x}_{\rm H\,I}$ constraints. In addition, the middle and bottom rows of our Figure 7, which show a preference for high $R_{\rm mfp}$ by the external constraints, are in agreement with the equivalent result in Greig & Mesinger (2017a).

The X-ray parameters from `21cmFAST` ($L_{\rm X<2\,keV}/{\rm SFR}$, E_0) and `Global21cm` ($f_{\rm X}$, $\nu_{\rm min}$) are not very sensitive to the external $\tau_{\rm e}$ and $\bar{x}_{\rm H\,I}$ estimates and therefore remain mainly constrained by the EDGES spectrum. Although in principle the two codes represent the same physical formalism, different assumptions and prior information lead to the exploration of different parameter ranges between M18 and here. Specifically, in M18 we explore scenarios where the IGM is heated by soft X-rays with (1) an X-ray spectral index $\alpha = -1$, (2) E_0 varying over 0.1–1.5 keV, and (3) an X-ray luminosity equivalent to $f_{\rm X}$ in the range $\sim3\times10^{-2}$–3×10^2. In this work we thoroughly probe a wider range of heating scenarios by exploring $f_{\rm X}$ in the range 10^{-5}–10^1 and $\nu_{\rm min}$ between 0.1 and 3 keV, assuming an X-ray spectral index $\alpha = -1.3$. A rough estimate, leaving aside the difference in the slope, low-energy cutoff, and X-ray energy range that goes into the definition of $L_{\rm X}$ ($E_0 - 10$ keV

in M18 versus $\nu_{\rm min} - 95$ keV here) shows that while in our models the combination $f_* f_{\rm X}$ varies between 10^{-8} and 5, an equivalent combination in M18 (with $f_* = 5\%$) varies between 1.6×10^{-4} and 1.6. Although in this paper we do explore soft X-ray scenarios equivalent to those in M18, our broader parameter ranges enable us to probe many more "cold IGM" cases. Moreover, because here we probe models up to higher values of $\nu_{\rm min}$, and that they extend to higher X-ray energy (out to 95 keV), on average our X-rays are harder and less efficient at heating than in M18. As a result, the global signals evaluated in this paper have, on average, deeper absorption troughs shifted to higher frequencies to which the EDGES High-Band spectrum is more sensitive. This enables us to derive the lower limits on $f_{\rm X}$ listed in Table 2.

Another aspect that leads to the differences in the X-ray constraints is the different range of $V_{\rm c}$ (equivalently, $T_{\rm vir}^{\rm min}$) explored in this paper (4.2–76.5 km s^{-1}) and in M18 (16.5–166 km s^{-1}). As the clearest example, Figure 2 of M18 shows regions of high probability for $T_{\rm vir}^{\rm min} \gtrsim 10^{5.2}$ K that occur at low $L_{\rm X<2\,keV}/{\rm SFR}$ and high E_0. These high-probability regions are mostly outside the parameter space of this paper as the high-end $V_{\rm c}$ cutoff here is lower. Thus, they are not projected to the marginalized X-ray PDFs of this paper. However, for $T_{\rm vir}^{\rm min} \lesssim 10^{5.2}$ K, the $L_{\rm X<2\,keV}/{\rm SFR} - T_{\rm vir}^{\rm min}$ and $E_0 - T_{\rm vir}^{\rm min}$ PDFs in Figure 2 of M18 do resemble the equivalent $f_{\rm X} - V_{\rm c}$ and $\nu_{\rm min} - V_{\rm c}$ PDFs in Figure 3 of this paper. This suggests that if a similar parameter space were explored, the constraints on parameters from `21cmFAST` and `Global21cm` would become more consistent.

6. Summary

We report new constraints on high-z astrophysical parameters derived from the EDGES High-Band measurement of the radio spectrum over 90–190 MHz (Monsalve et al. 2017b). We show that the spectrum is not only sensitive to reionization, i.e., the electron scattering optical depth and mean-free path of ionizing photons, but can also constrain processes of star formation and heating during cosmic dawn. Specifically, we place limits on the minimum circular velocity (equivalent to the minimum mass) of star-forming halos, the SFE, the X-ray efficiency of sources, and the low-energy cutoff of the X-ray SED. The definition and range of the parameters explored here correspond to the parameterization detailed in Cohen et al. (2017). The models were generated using the new `Global21cm` interpolation tool (A. Cohen et al. 2019, in preparation). These models represent traditional physical scenarios and do not include the exotic physics proposed to explain the EDGES Low-Band measurement (Bowman et al. 2018).

We compute the astrophysical parameter constraints within a Bayesian framework. First, we derive the constraints using the EDGES High-Band data alone. In this case the constraints depend on the sensitivity of the measurement—limited by noise and systematic uncertainty—to the spectral features of the 21 cm signal within the range 90–190 MHz, when simultaneously fitting a model that accounts for the foreground contribution. We then recompute the constraints after incorporating into the analysis a prior on the electron scattering optical depth from *Planck* (Planck Collaboration VI 2018) and estimates for $\bar{x}_{\rm H\,I}$ at $z \gtrsim 5.9$ from quasars (McGreer et al. 2015; Greig et al. 2017; Bañados et al. 2018) and LBGs (Mason et al. 2018).

Using EDGES data alone, and after marginalization over the foreground parameters and the residual astrophysical parameters, we disfavor at 68% confidence the following parameter ranges assuming a fixed $R_{\rm mfp} = 30$ Mpc:

1. High values of the minimum circular velocity of star-forming halos, $V_{\rm c} > 19.3$ km s^{-1}. This value corresponds to a minimum halo mass of $1.3 \times 10^8\,M_\odot$ at $z = 10$, which reflects that EDGES High-Band data are sensitive enough to constrain star formation in high-mass halos. Lower values of $V_{\rm c}$ generate 21 cm signals with absorption troughs at lower frequencies, which could be constrained more efficiently by Low-Band data.
2. Intermediate values of SFE, $0.4\% < f_* < 3.9\%$. Low values of f_* produce 21 cm signals that fall in the High-Band range but have low amplitude, while high values of f_* create troughs that are deep but wide. These types of signals cannot be disfavored with our current sensitivity.
3. Low values of the IGM X-ray heating efficiency, $f_{\rm X} < 0.0042$. After exploring a wide dynamical range of cosmic heating, we robustly disfavor a "cold IGM" scenario.
4. High values of the electron scattering optical depth, $\tau_{\rm e} > 0.08$, thus disfavoring early reionization.
5. High values of the X-ray SED low-frequency cutoff, $\nu_{\rm min} > 2.3$ keV, constraining the X-ray hardness of the early sources.

When fixing $\nu_{\rm min} = 0.5$ keV, the EDGES-only analysis also disfavors high values of the mean-free path of ionizing photons, $R_{\rm mfp} > 36.1$ Mpc.

Combining the EDGES High-Band data with the external observations primarily impacts the results for the parameters that most directly characterize the epoch of reionization: $\tau_{\rm e}$ and $R_{\rm mfp}$. However, due to the dependence of the reionization history on star formation, the constraint on $\tau_{\rm e}$ is degenerate with $V_{\rm c}$, in particular for $V_{\rm c} > 16.5$ km s^{-1}, i.e., the atomic hydrogen cooling scenario.

In the combined analysis we obtain the optical depth upper limit $\tau_{\rm e} < 0.063$ at 68% confidence. We find a similar limit, $\tau_{\rm e} < 0.064$, using only the neutral fraction estimates from quasars and LBGs. This reflects a broad agreement between independent observations despite the different models used for the redshift evolution of the neutral fraction. The EDGES contribution to the combined $\tau_{\rm e}$ constraint is marginal.

For $V_{\rm c}$, the combined analysis disfavors at 68% confidence the ranges $V_{\rm c} < 6.0$ km s^{-1} and $V_{\rm c} > 46.6$ km s^{-1}, while at 95%, it rules out $V_{\rm c} > 52.0$ km s^{-1}. This result indicates that EDGES High-Band + *Planck* + quasars + galaxies require the existence of halos with a minimum cooling mass below $2.5 \times 10^9\,M_\odot$ at $z = 10$. Interestingly, this is consistent with the EDGES absorption feature reported in Low-Band data, which requires efficient star formation in halos well below $10^{10}\,M_\odot$ (Mirocha & Furlanetto 2019).

The combined analysis reverses the shape of the $R_{\rm mfp}$ PDF relative to the result from EDGES data alone and assigns higher probabilities to higher values of this parameter, i.e., scenarios with faster growth of ionized bubbles and therefore faster reionization. Specifically, at 68% confidence we obtain the lower limit $R_{\rm mfp} > 27.5$ Mpc. Faster reionization scenarios are more compatible with the $\bar{x}_{\rm H\,I}$ upper limit at $z = 5.9$ from McGreer et al. (2015) combined with the reports of ongoing reionization at $z \gtrsim 7$ and a low optical depth.

Finally, the external observations do not significantly affect the results for the other astrophysical parameters, f_*, f_X, and ν_{min}, which remain mainly constrained by the EDGES High-Band spectrum.

The results of this paper are in broad agreement with the analyses of Greig & Mesinger (2017a) and Monsalve et al. (2018), which explored astrophysical models generated with the `21cmFAST` code (Mesinger & Furlanetto 2007; Mesinger et al. 2011). Nonetheless, noticeable differences occur with the results for V_c and the X-ray heating parameters in Monsalve et al. (2018). These discrepancies are primarily due to (1) making f_* a free parameter instead of fixing it at 5% as in Monsalve et al. (2018); (2) exploring a different range for V_c, which considers star formation in both atomic and molecular cooling halos; and (3) exploring wider ranges for f_X and ν_{min}, which extend to scenarios of very inefficient heating due to weak or hard X-ray sources.

We leave for future work detailed comparisons with results for models from `21cmFAST`, as well as analyses that incorporate measurements from EDGES Low-Band, which should increase the sensitivity to 21 cm signals whose main features lie below ~100 MHz.

We are grateful to Bradley Greig, Eduardo Bañados, and Charlotte Mason for providing us the hydrogen neutral fraction PDFs derived from quasar ULASJ1120+0641, quasar ULASJ1342+0928, and high-z galaxies, respectively. We also thank Bradley Greig, Kohei Inayoshi, Nicholas Kern, Andrei Mesinger, Jordan Mirocha, and the referee for useful comments and discussions. This work was supported by the NSF through research awards for the Experiment to Detect the Global EoR Signature (AST-0905990, AST-1207761, and AST-1609450). R.A.M. was supported by the NASA Solar System Exploration Virtual Institute cooperative agreement 80ARC017M0006, and by the NASA Ames Research Center grant NNX16AF59G. R.A.M. conducted part of this work at the Astrophysics and Cosmology Research Unit, University of KwaZulu-Natal, South Africa. A.F. is supported by the Royal Society University Research Fellowship. For R.B. and A.C., this publication was made possible by the ISF-NSFC joint research program (grant No. 2580/17) and through the support of a grant from the John Templeton Foundation; the opinions expressed in this publication are those of the authors and do not necessarily reflect the views of the John Templeton Foundation. Computations in this paper were run on the *Odyssey* cluster supported by the FAS Division of Science, Research Computing Group at Harvard University. EDGES is located at the Murchison Radio-astronomy Observatory. We acknowledge the Wajarri Yamatji people as the traditional owners of the Observatory site. We thank CSIRO for providing site infrastructure and support.

Software: Ipython (https://doi.org/10.1109/MCSE.2007.53), Numpy (https://doi.org/10.1109/MCSE.2011.37), Scipy (https://doi.org/10.5281/zenodo.1036423), Matplotlib (https://doi.org/10.5281/zenodo.573577), Astropy (The Astropy Collaboration et al. 2013), Healpy (Górski et al. 2005), h5py (https://doi.org/10.5281/zenodo.877338).

ORCID iDs

Raul A. Monsalve https://orcid.org/0000-0002-3287-2327
Anastasia Fialkov https://orcid.org/0000-0002-1369-633X
Judd D. Bowman https://orcid.org/0000-0002-8475-2036
Alan E. E. Rogers https://orcid.org/0000-0003-1941-7458
Thomas J. Mozdzen https://orcid.org/0000-0003-4689-4997
Nivedita Mahesh https://orcid.org/0000-0003-2560-8023

References

Ali, Z. S., Parsons, A. R., Zheng, H., Pober, J. C., et al. 2015, ApJ, 809, 61
Ali, Z. S., Parsons, A. R., Zheng, H., Pober, J. C., et al. 2018, ApJ, 863, 201
Alvarez, M. A., & Abel, T. 2012, ApJ, 747, 126
Bañados, E., Venemans, B. P., Mazzucchelli, C., et al. 2018, Natur, 553, 473
Barkana, R. 2016, PhR, 645, 1
Barkana, R. 2018, Natur, 555, 71
Barkana, R., & Loeb, A. 2001, PhR, 349, 125
Barkana, R., Outmezguine, N. J., Redigolo, D., & Volansky, T. 2018, PhRvD, 98, 103005
Beardsley, A. P., Hazelton, B. J., Sullivan, I. S., et al. 2016, ApJ, 833, 102
Behroozi, P. S., & Silk, J. 2015, ApJ, 799, 32
Berlin, A., Hooper, D., Krnjaic, G., & McDermott, S. D. 2018, PhRvL, 121, 011102
Bernardi, G., Zwart, J. T. L., Price, D., et al. 2016, MNRAS, 461, 2847
Bowman, J. D., Rogers, A. E. E., Monsalve, R. A., Mozdzen, T. J., & Mahesh, N. 2018, Natur, 555, 67
Ceverino, D., Glover, S. C. O., & Klessen, R. S. 2017, MNRAS, 470, 2791
Cohen, A., Fialkov, A., & Barkana, R. 2016, MNRAS, 459, L90
Cohen, A., Fialkov, A., Barkana, R., & Lotem, M. 2017, MNRAS, 472, 1915
Das, A., Mesinger, A., Pallottini, A., Ferrara, A., & Wise, J. H. 2017, MNRAS, 469, 1166
Davies, F. B., Hennawi, J. F., Bañados, E., et al. 2018, ApJ, 864, 142
Dowell, J., & Taylor, G. B. 2018, ApJL, 858, L9
Ewall-Wice, A., Chang, T.-C., Lazio, J., et al. 2018, ApJ, 868, 63
Ewall-Wice, A., Dillon, J. S., Hewitt, J. N., et al. 2016, MNRAS, 460, 4320
Feng, C., & Holder, G. 2018, ApJL, 858, L17
Fialkov, A., & Barkana, R. 2014, MNRAS, 445, 213
Fialkov, A., Barkana, R., & Cohen, A. 2018, PhRvL, 121, 011101
Fialkov, A., Barkana, R., Tseliakhovich, D., & Hirata, C. M. 2012, MNRAS, 424, 1335
Fialkov, A., Barkana, R., Visbal, E., Tseliakhovich, D., & Hirata, C. M. 2013, MNRAS, 432, 2909
Fialkov, A., Cohen, A., Barkana, R., & Silk, J. 2017, MNRAS, 464, 3498
Field, G. B. 1958, PIRE, 46, 240
Fixsen, D. J., Kogut, A., Levin, S., et al. 2011, ApJ, 734, 5
Fragos, T., Lehmer, B. D., Naoz, S., Zezas, A., & Basu-Zych, A. 2013, ApJL, 776, L31
Fraser, S., Hektor, A., Hütsi, G., et al. 2018, PhLB, 785, 159
Furlanetto, S. R., Oh, S. P., & Briggs, F. H. 2006, PhR, 433, 181
Gehlot, B. K., Mertens, F. G., Koopmans, L. V. E., et al. 2018, arXiv:1809.06661
Gilfanov, M., Grimm, H.-J., & Sunyaev, R. 2004, MNRAS, 347, L57
Górski, K. M., Hivon, E., Banday, A. J., et al. 2005, ApJ, 622, 759
Greig, B., & Mesinger, A. 2017a, MNRAS, 465, 4838
Greig, B., & Mesinger, A. 2017b, MNRAS, 472, 2651
Greig, B., Mesinger, A., & Bañados, E. 2019, MNRAS, 484, 5094
Greig, B., Mesinger, A., Haiman, Z., & Simcoe, R. 2017, MNRAS, 466, 4239
Grimm, H.-J., Gilfanov, M., & Sunyaev, R. 2003, MNRAS, 339, 793
Hektor, A., Hütsi, G., Marzola, L., et al. 2018, PhRvD, 98, 023503
Houston, N., Li, C., Li, T., Yang, Q., & Zhang, X. 2018, PhRvL, 121, 111301
Lehmer, B. D., Xue, Y. Q., Brandt, W. N., et al. 2012, ApJ, 752, 46
Ma, X., Hopkins, P. F., Garrison-Kimmel, S., et al. 2018, MNRAS, 478, 1694
Machacek, M. E., Bryan, G. L., & Abel, T. 2001, ApJ, 548, 509
Mashian, N., Oesch, P. A., & Loeb, A. 2016, MNRAS, 455, 2101
Mason, C. A., Trenti, M., & Treu, T. 2015, ApJ, 813, 21
Mason, C. A., Treu, T., Dijkstra, M., et al. 2018, ApJ, 856, 2
McGreer, I. D., Mesinger, A., & D'Odorico, V. 2015, MNRAS, 447, 499
McGreer, I. D., Mesinger, A., & Fan, X. 2011, MNRAS, 415, 3237
Mesinger, A. 2010, MNRAS, 407, 1328
Mesinger, A., & Furlanetto, S. R. 2007, ApJ, 669, 663
Mesinger, A., Furlanetto, S. R., & Cen, R. 2011, MNRAS, 411, 955
Mesinger, A., Greig, B., & Sobacchi, E. 2016, MNRAS, 459, 2342
Mineo, S., Gilfanov, M., & Sunyaev, R. 2012, MNRAS, 419, 2095
Mirabel, I. F., Dijkstra, M., Laurent, P., Loeb, A., & Pritchard, J. R. 2011, A&A, 528, 149
Mirocha, J., & Furlanetto, S. R. 2019, MNRAS, 483, 1980
Mirocha, J., Furlanetto, S. R., & Sun, G. 2017, MNRAS, 464, 1365
Mirocha, J., Mebane, R. H., Furlanetto, S. R., Singal, K., & Trinh, D. 2018, MNRAS, 478, 5591

Monsalve, R. A., Greig, B., Bowman, J. D., et al. 2018, ApJ, 863, 11
Monsalve, R. A., Rogers, A. E. E., Bowman, J. D., & Mozdzen, T. J. 2017a, ApJ, 835, 49
Monsalve, R. A., Rogers, A. E. E., Bowman, J. D., & Mozdzen, T. J. 2017b, ApJ, 847, 64
Mortlock, D., Warren, S. J., Venemans, B. P., et al. 2011, Natur, 474, 616
Mozden, T. J., Bowman, J. D., Monsalve, R. A., & Rogers, A. E. E. 2016, MNRAS, 455, 3890
Muñoz, J. B., Kovetz, E. D., & Ali-Haïmoud, Y. 2015, PhRvD, 92, 083528
Muñoz, J. B., & Loeb, A. 2018, Natur, 557, 684
Paciga, G., Albert, J. G., Bandura, K., et al. 2013, MNRAS, 433, 639
Pâris, I., Petitjean, P., Ross, N. P., et al. 2017, A&A, 597, A79
Patil, A. H., Yatawatta, S., Koopmans, L. V. E., et al. 2017, ApJ, 838, 65
Pentericci, L., Vanzella, E., Fontana, A., et al. 2014, ApJ, 793, 113
Planck Collaboration VI 2018, arXiv:1807.06209
Planck Collaboration XIII 2016, A&A, 594, A13
Planck Collaboration XVI 2014, A&A, 571, A16
Planck Collaboration XLVI 2016, A&A, 596, A107
Planck Collaboration XLVII 2016, A&A, 596, A108
Pritchard, J. R., & Loeb, A. 2008, PhRvD, 78, 103511
Read, J. I., Iorio, G., Agertz, O., & Fraternali, F. 2016, MNRAS, 462, 3628
Sikivie, P. 2019, PDU, 24, 100289
Singh, S., Subrahmanyan, R., Udaya Shankar, N., et al. 2017, ApJL, 845, L12
Singh, S., Subrahmanyan, R., Udaya Shankar, N., et al. 2018, ApJ, 858, 54
Subrahmanyan, R., & Cowsik, R. 2013, ApJ, 776, 42
Sun, G., & Furlanetto, S. R. 2016, MNRAS, 460, 417
Tashiro, H., Kadota, K., & Silk, J. 2014, PhRvD, 90, 083522
The Astropy Collaboration, Robitaille, T. P., Tollerud, E. J., et al. 2013, A&A, 558, A33
Tozzi, P., Madau, P., Meiksin, A., & Rees, M. J. 2000, ApJ, 528, 597
Varshalovich, D. A., & Khersonskii, V. K. 1977, SvAL, 3, 155
Visbal, E., Barkana, R., Fialkov, A., Tseliakhovich, D., & Hirata, C. M. 2012, Natur, 487, 70
Voytek, T. C., Natarajan, A., Jáuregui García, J. M., Peterson, J. B., & López-Cruz, O. 2014, ApJL, 782, L9
Wouthuysen, S. A. 1952, AJ, 57, 31
Xu, H., Wise, J. H., Norman, M. L., Ahn, K., & O'Shea, B. W. 2016, ApJ, 833, 84